Eigenvalue sensitivity, singular values and discrete frequency selection mechanism in noise amplifiers: the case of flow induced by radial wall injection

Stéphane Cerqueira[1],† **and Denis Sipp**[1]

[1]ONERA, The French AerospaceLab, 8 rue des Vertugadins, 92190 Meudon, France

We have performed linearized direct numerical simulations (DNS) of flow induced by radial wall injection forced by white-noise Gaussian forcings. We have shown that the frequency spectrum of the flow exhibits low-frequency discrete peaks in the case of a spatial structure of the forcing that is large scale. On the other hand, we observed that the spectrum becomes smooth (with no discrete peaks) if the spatial structure of the forcing is of a smaller extent. We have then tried to analyse these results in the light of global stability analyses. We have first computed the eigenvalue spectrum of the Jacobian and shown that the computed eigenvalues in the frequency range of interest were strongly damped and extremely sensitive to numerical discretization choices if large domains in the axial direction were considered. If shorter domains are used, then the eigenvalues are more robust but still extremely sensitive to the location of the upstream and downstream boundaries. Analysis of the ϵ-pseudo-spectrum showed that eigenvalues located in a region displaying 'background' values of ϵ below 10^{-12} were extremely sensitive and confirmed that all values in this region of the spectrum were actually quasi-eigenvalues. The eigenvalues are therefore ill-behaved and cannot be invoked to explain the observed discrete frequency selection mechanism. We have then performed a singular value decomposition of the global resolvent matrix to compute the leading optimal gains, optimal forcings and optimal responses, which are robust quantities, insensitive to numerical discretization details. We showed that the frequency response of the flow with the large-scale forcing can accurately be reproduced by an approximation based on the leading optimal gain/forcing/response. Analysis of this approximation showed that it is the projection coefficient of the forcing onto the leading optimal forcing that is responsible for the discrete frequency selection mechanism in the case of the large-scale forcing. From a more physical point of view, such a discrete behaviour stems from the streamwise oscillations of the leading optimal forcings, whose wavelengths vary with frequency, in combination with finite extent forcings (which start or end at locations where the leading optimal forcings are strong). Experimental results in the literature are finally discussed in light of these findings.

Key words: instability, shear layers, wakes/jets

† Email address for correspondence: stephane.cerqueira@airbus.com

1. Introduction

First discovered in the late 1930s, unsteady motions in solid propellant rocket motors were the first examples of combustion instabilities in propulsion systems (Culick 2006). Instabilities are generally observed during a firing as pressure oscillations in the combustion chamber growing spontaneously out of the noise. Pressure oscillations found in large solid rocket motors display low-level amplitudes and occur at frequencies close to longitudinal acoustic modes of the chamber.

Extensive work has been carried out to understand these pressure oscillations and has shown that sensitivity of burning surfaces to pressure and velocity fluctuations, and shedding of large-scale vortices interacting with acoustic waves are the chief possible causes of instabilities. In the case of large motors, as for instance in Ariane 5 boosters, the latter has been identified as the main origin for oscillation. According to Vuillot (1995), three forms of vortex shedding may exist in such motors. The first two arise from unstable shear layers (created by annular restrictor rings or the geometry of the grain) and the last is a consequence of the instability of the mean velocity profile. The present paper addresses this last point by analysing the hydrodynamic stability of the flow induced by wall injection.

Mean flows induced by wall injection are generally approximated by the self-similar analytical solution of the Euler equations with a slip condition at the head end of the chamber. This solution is referred to as the Taylor–Culick flow (Culick 1966; Taylor 1956) and has been widely used as base flow in previous hydrodynamic stability studies. The first stability analysis of the Taylor–Culick flow was performed by Varapaev & Yagodkin (1969) using local stability theory and considering a plane geometry. They demonstrated that the flow becomes unstable downstream of a critical abscissa. Casalis, Avalon & Pineau (1998) showed that such an analysis compared well with experimental data, while Griffond, Casalis & Pineau (2000) extended the local analysis to cylindrical geometries. The stability of the Taylor–Culick flow was finally addressed by Chedevergne, Casalis & Féraille (2006) using global stability theory, which accounts for the non-parallel effects. These authors found that the Taylor–Culick flow was globally stable (all of the eigenvalues of the global linearized Navier–Stokes operator are damped) but identified discrete stable global modes whose frequencies matched those measured in solid propellant rocket motors. As pointed out by Chedevergne (2007), the spectrum is found extremely sensitive to numerical details and exhibits convergence problems as the number of discretization points in the axial direction is increased. Chedevergne, Casalis & Majdalani (2012) showed that direct numerical simulations (DNS) initialized with such global modes evolve in accordance with the behaviour predicted by the linear stability analysis. Boyer, Casalis & Estivalèzes (2013a,b) showed that the eigenspectrum obtained when the computational domain is limited to a short section in the axial direction yields a spatially converged eigenvalue spectrum.

On the other hand, recent studies in stability theory (see Trefethen & Embree 2005; Sipp et al. 2010; Garnaud et al. 2013a) have shown that stable global modes do not constitute physically relevant quantities in open flows, especially if their damping rate is high. In particular, stable global modes often display a lack of robustness and may be very sensitive. This stems from the non-normality of the linear-evolution operator, which is due here to the downstream convection of the perturbations: the direct modes are localized downstream and the adjoint modes upstream, leading to nearly orthogonal direct and adjoint modes. Such a behaviour has been described early by Trefethen & Embree (2005) for toy models involving advection–diffusion operators combined with upstream and downstream boundary

conditions. This has led the stability community to consider other quantities than eigenvalues to describe the linear dynamics of stable flows. Trefethen *et al.* (1993) suggested to analyse transient-growth and pseudo-resonance mechanisms instead. Transient-growth mechanisms are best described by identifying optimal initial perturbations that lead to strongest energy growth at some given time T. In the frequency domain, pseudo-resonance mechanisms correspond to strong responses of the flow when the system is excited at some particular frequencies ω. To identify such pseudo-resonances, a singular value decomposition of the resolvent operator needs to be performed and, for each frequency, optimal forcings that yield the strongest response in the flow (the so-called optimal responses) are identified. Such analyses have first been carried out on simple laminar shear flows (Poiseuille, Couette flow, etc.) and more recently on their associated turbulent mean flows (McKeon & Sharma 2010; Moarref & Jovanović 2012; Sharma & McKeon 2013). More complex configurations, in which the streamwise direction is solved for (global stability analysis), have also been considered: backward-facing step flow (Blackburn, Barkley & Sherwin 2008; Marquet *et al.* 2008), boundary-layer flows (Alizard & Robinet 2007; Akervik *et al.* 2008; Monokrousos *et al.* 2010; Sipp *et al.* 2010; Sipp & Marquet 2012), homogeneous jet flows (Garnaud *et al.* 2013*b*), etc. Several studies pointed out the fact that stable eigenvalues are not the good quantities to focus on in the case of strongly convective flows (Sipp *et al.* 2010; Sipp & Marquet 2012; Garnaud *et al.* 2013*b*), either because they did not describe well the linear dynamics of the flow (Garnaud *et al.* 2013*a*) or because these modes were extremely sensitive (Barbagallo, Sipp & Schmid 2011).

The sensitivity of global modes in open flows is actually a timely issue that has been observed even in the case of globally unstable flows, such as a flow experiencing sudden expansion (Cantwell, Barkley & Blackburn 2010; Sanmiguel-Rojas, del Pino & Gutierrez-Montes 2010) or a jet in cross-flow (Ilak *et al.* 2012). The ϵ-pseudo-spectrum introduced by Trefethen *et al.* (1993), may actually be the best quantity to analyse this issue. It relies on the computation of the resolvent norm for frequencies lying in the complex plane. If the resolvent norm displays large values in a whole area around the computed eigenvalues, then these eigenvalues are extremely sensitive. Note that the resolvent norm, the optimal gains, optimal forcings and optimal responses are all robust quantities since they are obtained from a normal eigenproblem. The left and right eigenvectors being identical, the eigenvalue condition number is equal to 1. On the other hand, the global modes correspond to eigenmodes of the linearized Navier–Stokes operator, which may be strongly non-normal especially in the case of open flows due to convective non-normality. As mentioned above, the left and right eigenvectors tend to be orthogonal which may lead to extreme values of the eigenvalue condition number, and therefore trigger eigenvalue sensitivity.

The objective of the paper is to understand how discrete peaks can emerge in flow induced by radial wall injection. We will combine a series of tools to answer this question. First, we will try to find white-noise forcings for which linearized DNS simulations display discrete peaks in the frequency spectrum. We will also compute the frequency response of the flow in such cases to shed some light on this behaviour. Second, and as suggested by Chedevergne *et al.* (2006, 2012) and Boyer *et al.* (2013*a*,*b*), we will explore the 'eigenvalue' scenario: for this, we compute the spectrum of the Jacobian and assess the robustness of the stable eigenvalues by computing the ϵ-pseudo-spectrum of the flow. It is hoped here that weakly damped eigenvalues exist in the vicinity of the discrete peaks and that these eigenvalues are not too sensitive. Third, we will explore the 'optimal gain/forcing/response' scenario.

For this, we perform the singular value decomposition of the resolvent operator. Note that if there exist robust weakly damped eigenvalues in the vicinity of the discrete peaks ('eigenvalue' scenario), then the optimal gains should locally display overshoots, confirming that the eigenvalues of the Jacobian and the singular values of the resolvent are related quantities. Finally, we will analyse approximations of the resolvent operator based on the optimal gains/forcing/response quantities. If the frequency response displays discrete peaks at some given frequencies, then the approximations should reflect this behaviour: a careful analysis of the terms involved in the approximations should then help identify the term responsible for the discrete peaks.

The outline of the article is as follows. We will first (§ 2) present the configuration and the numerical techniques to spatially discretize the governing equations. The base flows will be presented in § 3 and compared to the inviscid Taylor–Culick solution. Then (in § 4), we will perform forced linearized DNS simulations and look for specific forcings, that are white in time but correlated in space, which produce frequency spectra with discrete peaks. Results of these simulations will be compared with the frequency response of the flow. Results pertaining to global modes for flow induced by radial wall injection will be discussed in § 5. In particular, we will assess the sensitivity of the computed eigenvalues by analysing the ϵ-pseudo-spectra. In § 6, we investigate the pseudo-resonances of the flow by computing the optimal gains, forcings and responses. In § 7, we consider the approximations of the frequency response based on the optimal quantities. We will try to identify the term which is responsible for the discrete peaks in the frequency response. Then (in § 8), we will compare the present results to those published in the literature for the VALDO experiment (see Cerqueira, Avalon & Feyel 2009). We will in particular (§ 9) propose a physical scenario based on the interaction of an acoustic wave and a wall defect to support the relevancy of the present theoretical approach. Concluding remarks are given in § 10.

2. Flow configuration, governing equations and spatial discretization

The configuration studied in this article focuses on flow induced by wall injection in an axisymmetric channel. It is a straightforward description of a cold gas apparatus, named VALDO (Cerqueira *et al.* 2009), commonly used for the study of pressure oscillation in Solid Propellant Rocket Motors. We will focus in the following on the dynamics of an axisymmetric flowfield, which may be justified by the following arguments. Using a local stability approach, Griffond *et al.* (2000) have shown that axisymmetric perturbations were always more unstable than non-axisymmetric perturbations, and that non-axisymmetric perturbations display an unstable region within the Reynolds-frequency space that is qualitatively similar to the one of the axisymmetric perturbations. Also, in the VALDO experiment, since no azimuthal velocity fluctuations measurements have been performed, it is difficult to assess the importance of non-axisymmetric fluctuations. At this stage, there is therefore no strong evidence indicating that such perturbations should behave differently from axisymmetric ones. Such considerations led several authors, see Chedevergne *et al.* (2006) and Boyer *et al.* (2013*a*), to only consider axisymmetric perturbations in their analyses.

The flow field is described in a cylindrical coordinate system (figure 1). The state vector $\boldsymbol{q}$ stands for the flowfield $(\boldsymbol{u}, p)^*$ where * designates the conjugate transpose and $\boldsymbol{u} = (u_r, u_z)$ designate the radial and axial components of the velocity. Variables are non-dimensionalized using the pipe radius R and the wall injection velocity V_{inj}.
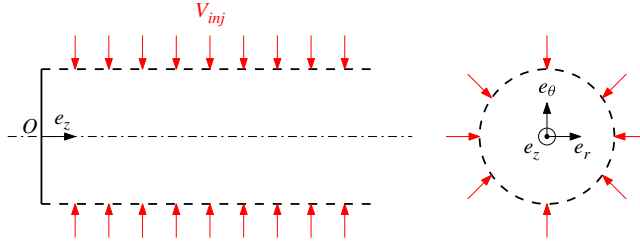
FIGURE 1. (Colour online) Cylindrical coordinate system (r, θ, z). The head-end is located at $z = 0$ and the (red online) arrows symbolize the flow sidewall injection.

The fluid motion is governed by the forced axisymmetric incompressible Navier–Stokes equations that read

$$\boldsymbol{\nabla} \cdot \boldsymbol{u} = 0, \quad \partial_t \boldsymbol{u} + \boldsymbol{u} \cdot \boldsymbol{\nabla} \boldsymbol{u} + \boldsymbol{\nabla} p - Re^{-1} \nabla^2 \boldsymbol{u} = \epsilon \boldsymbol{f}' \qquad (2.1a,b)$$

where Re is the Reynolds number based on R, V_{inj} and the kinematic viscosity. The term $\epsilon \boldsymbol{f}'$ is a small-amplitude unsteady volumic source term, that represents noise in the system. In the following, we will consider three Reynolds numbers, $Re = 1600$, 2075, 2290, which are relevant for a cold-gas apparatus such as the VALDO set-up. The boundary conditions are as follows:

$$\left. \begin{array}{ll} \boldsymbol{u} = (-1, 0) & \text{on } \varGamma_{in} \\ \boldsymbol{u} = \boldsymbol{u}(r) & \text{on } \varGamma_w \\ -p\boldsymbol{n} + Re^{-1} \boldsymbol{\nabla} \boldsymbol{u} \cdot \boldsymbol{n} = \boldsymbol{0} & \text{on } \varGamma_{out} \\ u_r = \partial_r u_z = 0 & \text{on } \varGamma_a, \end{array} \right\} \qquad (2.2)$$

which stand for fluid wall injection at $\varGamma_{in}$, prescribed velocity profile $\boldsymbol{u}(r)$ at the left boundary $\varGamma_w$, no-stress condition at the outlet $\varGamma_{out}$ and a condition for the flow to be axisymmetric at $\varGamma_a$. The prescribed velocity profile is zero $\boldsymbol{u}(r) = 0$ (no-slip condition) if the computational domain starts at the head end ($z_b = 0$); if not ($z_b > 0$), a prescribed velocity profile $\boldsymbol{u}(r) = 0$ needs to be determined (for example, by interpolation from an existing flow defined in the entire channel) and applied at $\varGamma_w$.

The flow solution is decomposed into a base flow $(U_r, U_z, P)^{\mathrm{T}}$ and a small-amplitude unsteady disturbance denoted by $\epsilon \boldsymbol{q}'$ with $\boldsymbol{q}' = (u_r', u_z', p')^{\mathrm{T}}$. After introducing this decomposition into (2.1), we obtain at leading order the equations defining the base flow:

$$\boldsymbol{\nabla} \cdot \boldsymbol{U} = 0, \quad \boldsymbol{\nabla} \boldsymbol{U} \cdot \boldsymbol{U} + \boldsymbol{\nabla} P - Re^{-1} \nabla^2 \boldsymbol{U} = 0, \qquad (2.3a,b)$$

with the same boundary conditions as above.

At the next order in ϵ, we obtain the equations governing the perturbation:

$$\boldsymbol{\nabla} \cdot \boldsymbol{u}' = 0, \quad \partial_t \boldsymbol{u}' = -\boldsymbol{\nabla} \boldsymbol{U} \cdot \boldsymbol{u}' - \boldsymbol{\nabla} \boldsymbol{u}' \cdot \boldsymbol{U} - \boldsymbol{\nabla} p' + Re^{-1} \nabla^2 \boldsymbol{u}' + \boldsymbol{f}', \qquad (2.4a,b)$$

with again the same boundary conditions as before, except $\boldsymbol{u}' = \boldsymbol{0}$ at the injecting wall $\varGamma_{in}$ and at the left boundary $\varGamma_w$.

All equations are spatially discretized with a finite-element method. The mesh structure is depicted in figure 2. Its refinement is controlled by the vertex densities $n_1 = 70$ (dashed line), $n_2 = 100$ (thin solid line) and $n_3 = 140$ (thick solid line) on
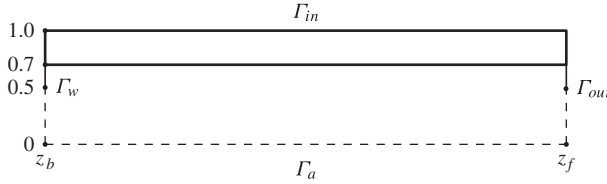
FIGURE 2. Mesh structure: z_b and z_f denote, respectively, the location of the left Γ_w and right Γ_{out} boundaries of the computational domain. Here Γ_{in} and Γ_a represent the injecting wall and the axis of symmetry. The dashed, thin solid and thick solid lines are characterized by the vertex densities $n_1 = 70$, $n_2 = 100$ and $n_3 = 140$, respectively.

Discretization	z_b	z_f	n_t	Discr. type	$n_{d.o.f.}$	Boundary condition Γ_w
D_1	0	11	291 092	P1b × P1b × P1	1 022 578	No-slip
D_2	0	14	372 920	P1b × P1b × P1	1 309 921	No-slip
D_3	0	11	291 092	P2 × P2 × P1	1 316 172	No-slip
D_4	4	8	104 854	P1b × P1b × P1	368 540	Interp. from D_1
D_5	4	9	133 342	P1b × P1b × P1	468 563	Interp. from D_1
D_6	3	9	157 424	P1b × P1b × P1	553 165	Interp. from D_1
D_7	3	8	133 360	P1b × P1b × P1	468 626	Interp. from D_1

TABLE 1. Different spatial discretizations: z_b and z_f are the locations of the left and right boundaries; n_t is the number of triangles, 'Discr. type' is the type of finite elements to represent (u_r, u_z, p), while $n_{d.o.f.}$ is the number of degrees of freedom of an unknown (u_r, u_z, p). The boundary condition applied at Γ_w depends on the location of the left boundary Γ_w and is specified in the last column.

both external and internal boundaries. The spatial extent of the meshes is governed by the abscissa z_b and z_f of the left and right boundaries, the head end of the chamber being located at $z = 0$.

The unknown velocity and pressure fields are represented either with Arnold–Brezzi–Fortin MINI elements (see Matsumoto & Kawahara 2000), having four-node P1b elements for the velocity components and three-node P1 elements for the pressure, or with Taylor–Hood elements, having six-node P2 elements for the velocity and three-node P1 elements for the pressure. These spatial discretizations are respectively first- and second-order accurate. Momentum and continuity equations are first multiplied by r^2 and r to avoid the singularity on the $r = 0$ axis. The associated variational formulations are then derived, and the discretized equations obtained for seven distinct cases: D_1 and D_3 are based on the same mesh starting at $z_b = 0$ and extending up to $z_f = 11$ but with different spatial discretizations (first order for D_1, second order for D_3); D_1 and D_2 display the same spatial first-order discretization but extend up to $z_f = 11$ and $z_f = 14$, respectively, the left boundary being located at the head end $z_b = 0$; D_4, D_5, D_6 and D_7 are all first order but start and end at different locations $z_b = 3$ or 4 and $z_f = 8$ or 9. The number of degrees of freedom for an unknown (u_r, u_z, p) involved in each case is given in table 1.

The equation governing the perturbation (2.4) may then be reformulated in discrete form as

$$\boldsymbol{B}\frac{\mathrm{d}\boldsymbol{q}'}{\mathrm{d}t} = \boldsymbol{A}\boldsymbol{q}' + \boldsymbol{PM}f', \tag{2.5}$$
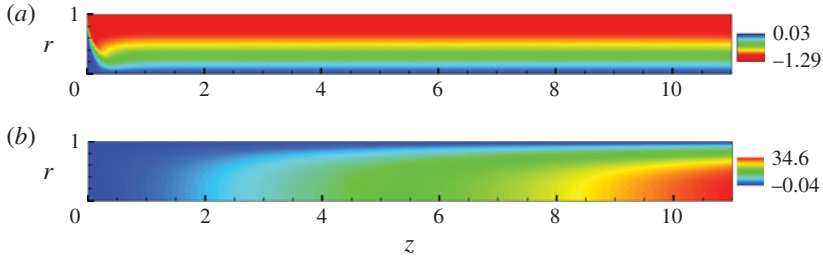
FIGURE 3. Base flow at $Re = 1600$. Isocontours of radial velocity (*a*) and axial velocity (*b*). Discretization D_1.

where $\textbf{\textit{A}}$, $\textbf{\textit{B}}$, $\textbf{\textit{M}}$ and $\textbf{\textit{P}}$ are sparse large-scale matrices. Here, $\textbf{\textit{B}}$ is defined by $\textbf{\textit{B}} = \textbf{\textit{PMP}}^*$, $\textbf{\textit{M}}$ designates the mass matrix, which acts solely on the velocity components, $\textbf{\textit{P}}$ is the prolongation matrix, which takes a velocity vector and adds zero pressure components to yield a velocity–pressure vector and $\textbf{\textit{P}}^*$ corresponds to the restriction operator, which extracts the velocity components from a velocity–pressure vector.

3. Base flow

The base flows, which are solutions of (2.3), have first been determined for discretizations D_1, D_2 and D_3, for which the boundary condition at Γ_w corresponds to no-slip ($z_b = 0$). Then, the base flows for D_4, D_5, D_6 and D_7, which all start at $z_b > 0$, may be computed by considering the radial velocity profile at section z_b obtained in the D_1 base flow (see the boundary condition at Γ_w given in last column of table 1). The zeros of the nonlinear equations (2.3) are obtained thanks to an iterative Newton method, in which the matrix inversions were handled by a direct sparse LU parallel solver (MUMPS package, http://graal.ens-lyon.fr/MUMPS, see Amestoy *et al.* (2001)). This iterative process is carried out until the vector two-norm of the residual of the governing equations becomes smaller than 10^{-12}. Figure 3 shows isocontours of the base flow computed at $Re = 1600$ for discretization D_1.

Accuracy of the numerical method is assessed by comparing the computed base flow with the Taylor–Culick analytical solution (Culick 1966; Taylor 1956) for an axisymmetric flow induced by wall injection in a channel:

$$\begin{aligned} \textbf{\textit{U}} &= U_r \textbf{\textit{e}}_r + U_z \textbf{\textit{e}}_z, \\ &= -\frac{1}{r} \sin\left(\frac{\pi r^2}{2}\right) \textbf{\textit{e}}_r + \pi z \cos\left(\frac{\pi r^2}{2}\right) \textbf{\textit{e}}_z. \end{aligned} \tag{3.1}$$

We recall that the Taylor–Culick analytical solution does not take into account the no-slip condition at the head end of the chamber. Therefore some mismatch is expected in this area that should decrease as we move away from the head-end. We verified that the base-flow obtained at $Re = 1600$ displays an excellent agreement with the Taylor–Culick analytical solution for an abscissa $z > 2$ (see figure 4). Note that this also holds for higher Reynolds numbers ($Re = 2075$, 2290). Such results are in accordance with those obtained recently by Chedevergne *et al.* (2012).

4. Discrete frequency selection mechanism with white noise forcing: a DNS study

In this section, we carry out a numerical experiment to show that flow induced by radial wall injection is globally stable and that such a flow may present unsteadiness
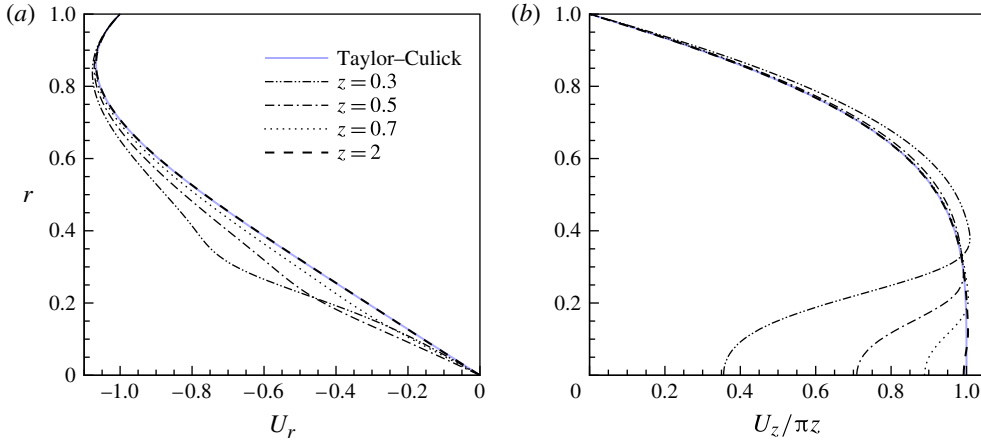
FIGURE 4. (Colour online) Base-flow at $Re = 1600$. Radial U_r (a) and axial U_z (b) velocity profiles. The head-end boundary layer is emphasized. Discretization D_1.

displaying a series of well-defined peaks in the frequency spectrum in presence of white noise Gaussian forcing.

For this, we perform for $Re = 1600$ (with discretization D_1) forced linearized DNS simulations by integrating in time (2.5) and by considering a forcing of the form

$$\boldsymbol{f}' = n(t)\hat{\boldsymbol{f}}(r, z) = n(t) \begin{pmatrix} \hat{f}_r(r, z) \\ \hat{f}_z(r, z) \end{pmatrix} \tag{4.1}$$

where $n(t)$ is a zero-mean white Gaussian forcing of unit standard deviation. Two distinct spatial forcing structures $\hat{\boldsymbol{f}}(r, z)$ will be considered. The first is large scale in z with $\hat{f}_z = 0$ and $\hat{f}_r = 1$ within $(0.90 \leqslant r \leqslant 0.95, 2 \leqslant z \leqslant 6)$ and 0 outside. The second is similar but less extended in the z direction: $\hat{f}_z = 0$ and $\hat{f}_r = 1$ within $(0.90 \leqslant r \leqslant 0.95, 3.85 \leqslant z \leqslant 4.15)$ and 0 outside. In the rest of the paper, these two specific forcings will respectively be referred to as the large-scale and narrow forcings.

From a numerical point of view, we temporally discretize (2.5) thanks to a fully implicit second-order backward-finite-difference method:

$$\alpha_0 \boldsymbol{Bq}^{m+1} + \alpha_1 \boldsymbol{Bq}^m + \alpha_2 \boldsymbol{Bq}^{m-1} = \boldsymbol{Aq}^{m+1} + \beta_1 \boldsymbol{PMf}^m + \beta_2 \boldsymbol{PMf}^{m-1}, \tag{4.2}$$

with $\alpha_0 = 1.5/\Delta t$, $\alpha_1 = -2/\Delta t$, $\alpha_2 = 0.5/\Delta t$, $\beta_1 = 2/\Delta t$ and $\beta_2 = -1/\Delta t$ and m as the time index. The matrix inverses are carried out at each time step by a direct LU solver (UMFPACK package, http://cise.ufl.edu/research/sparse/umfpack/, see Davis & Duff (1997)). We used $\Delta t = 1/5000$ for discretization D_1 to keep the CFL number below 1. The time discretization of (2.5) with the forcing defined in (4.1) induces that the high-frequency part ($\omega > \pi/\Delta t \approx 15\,700$) of the exciting noise $n(t)$ is discarded. This is not an issue since the frequencies of interest in the flowfield are much lower $\omega < 200$.

Simulations for both forcing structures evolve toward a statistically steady state. As a consequence, one may infer that the considered base flow is stable (in a linear set-up, a globally unstable flow leads to diverging signals, which is not the case here), in agreement with previous studies (Chedevergne *et al.* 2006). We have represented
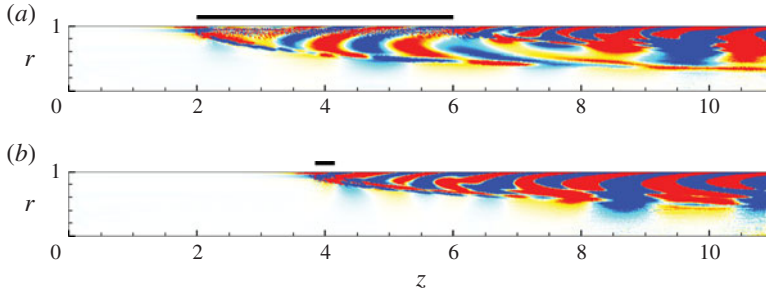
FIGURE 5. Typical azimuthal-vorticity snapshots of perturbation from linearized forced DNS simulations after the transient has passed away (in the statistically steady state): (*a*) large-scale forcing; (*b*) narrow forcing. Here $Re = 1600$, discretization D_1. The horizontal straight line above each plot indicates the streamwise extent of the spatially coherent forcing.

in figure 5 typical snapshots of the flow obtained in this asymptotic regime. We can see in both simulations large-scale vortical structures associated with low frequencies. A frequency-selection mechanism is therefore at play since the white noise forcing injects an equal amount of energy in all frequencies. Note that the vortical structures emerging in the vicinity of the injecting wall are similar to those computed by Vuillot (1995). Such vortices are characteristic of the instability of flow induced by wall injection. In both figures, one may observe small wiggles in the vicinity of the forcing structure $\hat{f}(r, z)$. These are linked to the small-scale perturbations triggered by the forcing injected at high frequencies.

We now analyse the frequency content of the unsteadiness. For this, we have computed the spectrum of the z component of the velocity field at two different points located far downstream of the two forcing regions: one near the injecting wall at $(r_c = 0.9, z_c = 8)$ and one at the centreline of the channel at $(r_c = 0, z_c = 8)$. We have represented the spectra of these two signals (cyan and magenta thick lines) in figure 6 for the large-scale (*a*) and narrow (*b*) forcing cases. These spectra have been obtained by analysing the input signal $n(t)$ defined in (4.1) and the output signals $u_z(t)$ obtained near the injecting wall and at the centreline of the channel. We have represented the quantity $\sqrt{|P_{nu_z}/P_{nn}|}$, where P_{nu_z} is the cross-power spectral density of n and u_z and P_{nn} is the power spectral density of n. Here P_{nu_z} and P_{nn} have been obtained using a Welch method, with 11 overlapping (50 %) segments of 40 000 samples, which leads to a resolution of $\Delta\omega = 0.79$. It appears that the frequency spectra for the large-scale forcing (figure 6*a*) display a series of peaks regularly spaced in the frequency range $40 < \omega < 80$. The peaks are located at the same frequencies for the spectra obtained near the injecting wall and at the centreline of the channel. These peaks are due to large-scale motions, whose characteristic size scales on the radius of the channel. For the narrow forcing (figure 6*b*), the result is different: at all spatial locations, the frequency spectrum displays a single large hump around the frequencies $40 < \omega < 80$. Therefore, no discrete series of peaks are observed in this case, indicating that the discrete frequency selection mechanism observed in figure 6(*a*) depends on the spatial structure that excites the flow. Note that the noise has been chosen delta correlated in time (white noise) in these DNS. This choice has been made for convenience to obtain a flat broadband exciting spectrum for $n(t)$; yet, only a broadband exciting noise in the frequency range $0 < \omega < 100$ (which may be more correlated in time) is actually required to produce similar results.
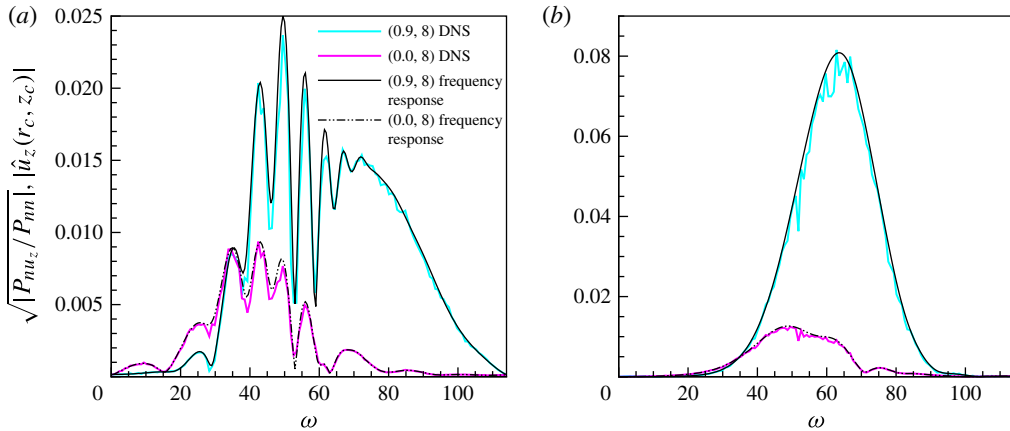
FIGURE 6. Spectrum of the u_z component near the injecting wall ($r_c = 0.9$, $z_c = 8$) and at the centreline of the channel ($r_c = 0$, $z_c = 8$) with large-scale forcing (*a*) and narrow forcing (*b*). Here $Re = 1600$, discretization D_1.

The spectra presented in figure 6 actually also correspond to the transfer functions from the signal n to the z component of the velocity fields at the different spatial locations that were introduced above. These transfer functions may therefore also be evaluated by computing the frequency response of the linear input–output system. For a harmonic forcing of the form $\hat{f}' = e^{i\omega t}\hat{f}$, with the large-scale or narrow forcing $\hat{f}$ defined above, the frequency response consists of determining the sustained asymptotic response $\hat{u}' = e^{i\omega t}\hat{u}$, where $\hat{u}$ is the solution of

$$\hat{u} = R(\mu)\hat{f}. \tag{4.3}$$

Here $R = P^*(\mu B - A)^{-1}PM$ is the global resolvent matrix and $\mu = i\omega$ is a complex scalar related to the considered frequency. We may compute $\hat{u}$ for any frequency ω by solving the linear system in (4.3). This was done here by use of the direct sparse LU solver MUMPS. We have shown in figure 6(*a*,*b*) (see black thin lines) the values of $|\hat{u}(r_c, z_c)|$ evaluated at the two spatial locations introduced above as a function of frequency. We observe that these curves are very close to the frequency spectra obtained by time-averaging (blue and red thick lines). This good agreement shows that the spectra obtained by time-averaging are well converged and that the discrete peaks observed in figure 6(*a*) may fully be accounted for by an analysis of the frequency response of the flow $\hat{u}$. In the following, we will try to understand which properties of the resolvent R may explain these observations. We will investigate two possibilities. The first, already advocated by Chedevergne *et al.* (2006), suggests that weakly damped eigenmodes of A may exist in the vicinity of these frequencies. The second consists of analysing the singular values and modes of the resolvent R and to look for pseudo-resonances. This has already been achieved in other globally stable flows, such as boundary layers and jets. Yet, in all of these configurations, no discrete frequency selection mechanism characterized by a spiky frequency spectrum has been reported. Note that these two ways of analysing the dynamics is of course related: if weakly damped global modes exist in the vicinity of some discrete frequencies, then the singular values should display an overshoot near these frequencies.

5. Eigenvalue spectrum and ϵ-pseudo-spectrum for flow induced by radial wall injection

5.1. *Eigenvalues*

When considering perturbations under the form $\boldsymbol{q}' = \hat{\boldsymbol{q}} e^{\mu t}$, (2.5) yields for zero external forcing $\boldsymbol{f}' = 0$:

$$\boldsymbol{A}\hat{\boldsymbol{q}} = \mu \boldsymbol{B}\hat{\boldsymbol{q}}. \qquad (5.1)$$

The eigenvalues μ are complex and their real and imaginary parts respectively refer to the amplification rate σ and frequency ω of the mode. Eigenvalues are obtained in the vicinity of some complex shift parameter s by looking for the eigenvalues of largest magnitude of $(\boldsymbol{A} - s\boldsymbol{B})^{-1}\boldsymbol{B}$. A power-method consists in repeatedly applying the latter matrix on a given vector. The use of Krylov subspaces improves the convergence of such a method and allows to extract multiple eigenvalues. In the present study, we used the ARPACK library (http://www.caam.rice.edu/software/ARPACK) in combination with the sparse direct LU solver of the MUMPS package to extract a series of eigenvalues near some complex shift s.

We have investigated the eigenvalue spectrum of the flow for the seven discretizations D_1–D_7 introduced in §2. We considered 11 different shifts $s = 0, 10i, 20i, \ldots,$ $100i$ and computed in each case 20 eigenvalues that were closest to the shift. For $Re = 1600$, we have reported the results in figure 7(a–c) for the discretizations D_1, D_2 and D_4. We first focus on figure 7(a), which is concerned with discretization D_1, i.e. $z_b = 0$, $z_f = 11$ and a first-order spatial discretization. We observe that all eigenvalues display a negative amplification rate σ and that the damping rate is very strong for values of the frequency $\omega > 20$. The computed eigenvalues should be independent of the shift parameters s that were used. While a perfect match is obtained at low frequencies ($\omega \leqslant 30$), we observe that this is no longer the case at higher frequencies ($\omega > 30$), see the inset to figure 7(a) showing a zoom of such a region. We can see that each shift s yields different eigenvalues, which all display similar damping rates around $-\sigma \approx 15$. Same behaviour has been observed in the thesis of Chedevergne (2007) when the number of Chebyshev points is increased in the axial direction. Final results in his work were obtained with a correct resolution in the radial direction but a coarse resolution in the axial direction. These under-resolved results were presented in Chedevergne *et al.* (2006) and Chedevergne *et al.* (2012).

Results displaying non-overlapping eigenvalues for different shifts are not common in the literature. In the case of boundary layers, which are also globally stable flows, the least-damped eigenvalues representing Tollmien–Schlichting waves were not found to be very sensitive (see Ehrenstein & Gallaire 2005; Alizard & Robinet 2007; Akervik *et al.* 2008). In the case of an open cavity flow, Barbagallo, Sipp & Schmid (2009), Barbagallo *et al.* (2011) showed that strongly damped global modes were difficult to compute and dependent on the shift value. This behaviour was well explained by the advection–diffusion model problem introduced by Trefethen & Embree (2005).

Figure 7(b,c) show the eigenvalue spectrum for a computational domain extended up to $z_f = 14$ while keeping $z_b = 0$ (discretization D_2) and a domain reduced to the slice $z_b = 4 \leqslant z \leqslant 8 = z_f$ (discretization D_4). We can see that the results are qualitatively similar in the case of the larger domain (discretization D_2) with overlapping eigenvalues at low frequencies, non-overlapping eigenvalues at high frequencies. The only difference lies in the fact that the damping rate of the high-frequency eigenmodes has slightly decreased to $-\sigma \approx 11$. In the case of a shorter axial domain, the situation is radically different: the low-frequency eigenvalues ($\omega < 40$) have disappeared and the
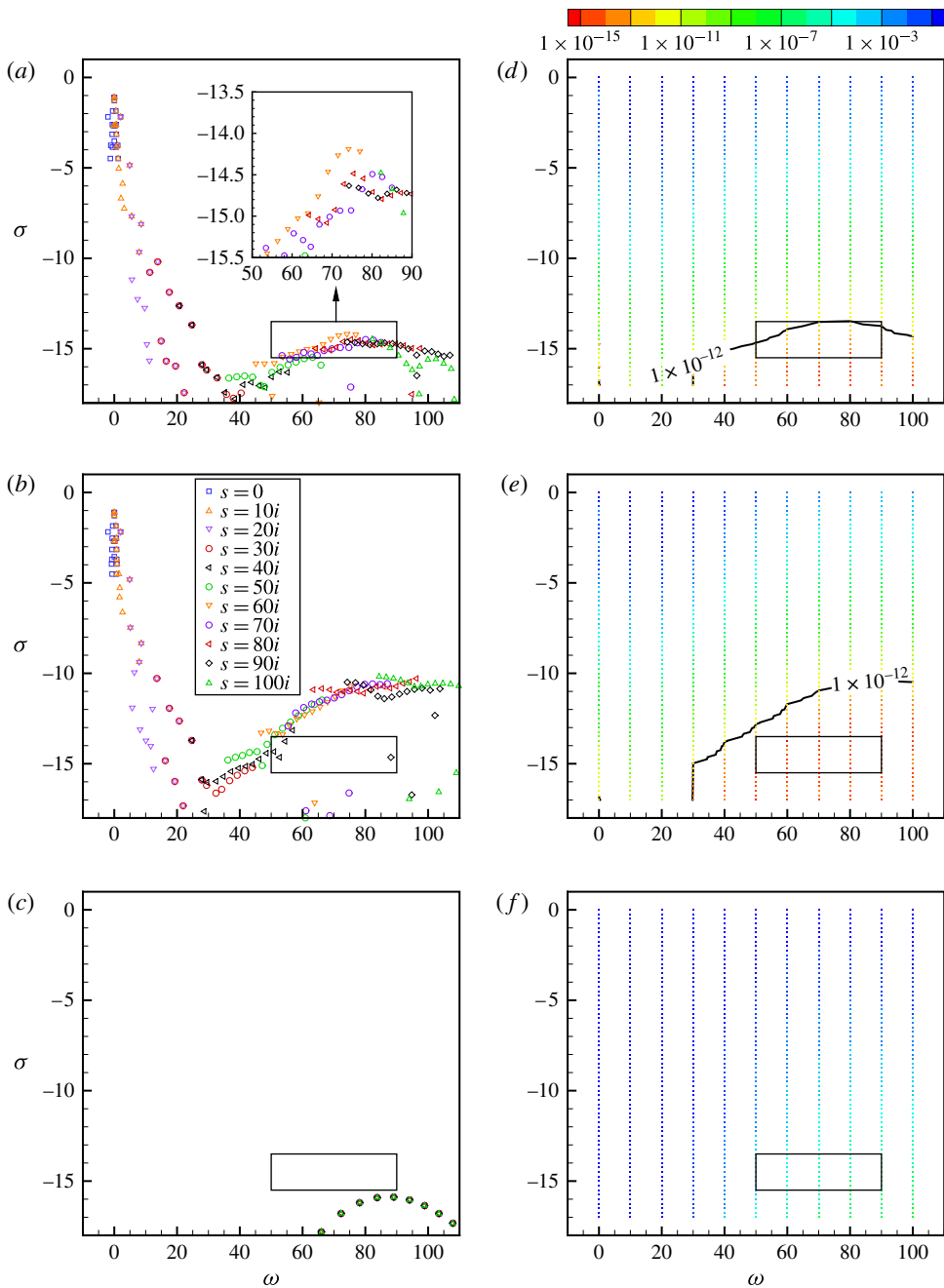
FIGURE 7. (*a–c*) Eigenvalue spectra in the (ω, σ) plane obtained with discretizations D_1, D_2 and D_4, respectively. Colours indicate eigenvalues computed with distinct shift parameters s (shown in *b*). (*d–f*) Corresponding ϵ-pseudo-spectra in the (ω, σ) plane. Here $Re = 1600$. In (*a*), the inset corresponds to a zoom of the represented rectangle. In all other panels, we have drawn the same rectangle to ease comparison. In (*d,e*), the solid line refers to the isovalue $\epsilon = 10^{-12}$.

high-frequency modes ($\omega > 40$) are now clearly defined with overlapping eigenvalues obtained for distinct shifts. We have checked that we precisely recover the spectrum given by Boyer *et al.* (2013b) who used spectral discretization and the same outlet boundary condition.

5.2. ϵ-pseudo-spectrum

5.2.1. *Definition and computation*

The governing equations (2.5) may be recast in state-space form by eliminating the pressure p':

$$\frac{\mathrm{d}\boldsymbol{u}'}{\mathrm{d}t} = \widetilde{\boldsymbol{A}}\boldsymbol{u}' + \boldsymbol{f}'. \tag{5.2}$$

The matrix $\widetilde{\boldsymbol{A}}$ only acts on the velocity field and corresponds to the matrix $\boldsymbol{A}$ projected on the divergence-free subspace. In this expression, we assumed that the forcing $\boldsymbol{f}'$ is divergence-free. The resolvent matrix associated with $\widetilde{\boldsymbol{A}}$ is $\widetilde{\boldsymbol{R}} = (\mu\widetilde{\boldsymbol{I}} - \widetilde{\boldsymbol{A}})^{-1}$. The norm of the matrix $\widetilde{\boldsymbol{R}}$ is given by

$$\|\|\widetilde{\boldsymbol{R}}\|\|_{\boldsymbol{Q}} = \max_{\hat{f}} \frac{\hat{\boldsymbol{f}}^* \widetilde{\boldsymbol{R}}^* \boldsymbol{Q}\widetilde{\boldsymbol{R}}\hat{\boldsymbol{f}}}{\hat{\boldsymbol{f}}^* \boldsymbol{Q}\hat{\boldsymbol{f}}}, \tag{5.3}$$

where the maximum is searched for in the divergence-free subspace and $\boldsymbol{Q}$ is chosen to represent the following scalar product:

$$\boldsymbol{u}^* \boldsymbol{Q}\boldsymbol{v} = \int_{\Omega} (\bar{u}_r v_r + \bar{u}_z v_z) r \, \mathrm{d}r \, \mathrm{d}z. \tag{5.4}$$

The integral is taken over the whole computational domain.

The resolvent norm $\|\|\widetilde{\boldsymbol{R}}(\mu)\|\|_{\boldsymbol{Q}}$ is infinite for values of μ corresponding to eigenvalues of $\widetilde{\boldsymbol{A}}$. Furthermore, Trefethen *et al.* (1993) showed that an arbitrary complex μ corresponds to an eigenvalue of a perturbed matrix $\widetilde{\boldsymbol{A}} + \delta\widetilde{\boldsymbol{A}}$ for a sufficiently large perturbation matrix $\delta\widetilde{\boldsymbol{A}}$. It may be shown that the critical size of this perturbation matrix $\delta\widetilde{\boldsymbol{A}}$ is given by $\|\|\delta\widetilde{\boldsymbol{A}}\|\|_{\boldsymbol{Q}} = 1/\|\|\widetilde{\boldsymbol{R}}(\mu)\|\|_{\boldsymbol{Q}}$. Hence, if $\|\|\widetilde{\boldsymbol{R}}(\mu)\|\|_{\boldsymbol{Q}}$ is very large (say $\|\|\widetilde{\boldsymbol{R}}(\mu)\|\|_{\boldsymbol{Q}} \approx 10^{15}$), then there exists a very small perturbation matrix $\delta\widetilde{\boldsymbol{A}}$ (say $\|\|\delta\widetilde{\boldsymbol{A}}\|\| \approx 10^{-15}$) such that μ is an eigenvalue of $\widetilde{\boldsymbol{A}} + \delta\widetilde{\boldsymbol{A}}$. In this case μ is a quasi-eigenvalue of $\widetilde{\boldsymbol{A}}$. The matrix perturbation $\delta\widetilde{\boldsymbol{A}}$ may stem from various origins: discretization scheme, mesh refinement, imperfection in the geometry, location of the outlet boundary, nature of downstream boundary condition, etc.

One may finally show that the eigenvalues of $\widetilde{A}$ are the same as those obtained for the generalized eigenproblem ($\boldsymbol{A}, \boldsymbol{B}$) defined in (5.1) and that

$$\|\|\widetilde{\boldsymbol{R}}(\mu)\|\|_{\boldsymbol{Q}} = \lambda_1(\mu), \tag{5.5}$$

where $\lambda_1(\mu)^2$ corresponds to the largest eigenvalue of the eigenproblem that will be introduced below in (6.2) with $\boldsymbol{Q}_u = \boldsymbol{Q}_f = \boldsymbol{Q}$.

5.2.2. *Results*

In the following, we will analyse the ϵ-pseudo-spectrum of the flow, which consists of plotting the quantity $\epsilon = \|\|\widetilde{\boldsymbol{R}}(\mu)\|\|_{\boldsymbol{Q}}^{-1}$ in the (ω, σ) plane. At each point of the plane

$\mu = \sigma + i\omega$, the quantity ϵ corresponds to the critical size of the perturbation matrix $\||\delta\widetilde{\boldsymbol{A}}|\|_{\boldsymbol{Q}}$ so that μ is an eigenvalue of $\widetilde{\boldsymbol{A}} + \delta\widetilde{\boldsymbol{A}}$. Note that the ϵ-pseudo-spectrum is a robust quantity contrary to the eigenvalues of $\widetilde{\boldsymbol{A}}$, which are likely to be prone to ill-conditioning.

We now analyse the ϵ-pseudo-spectra introduced in §5.2. We have shown in figure 7(*d*) the quantity ϵ (in logarithmic scale) for discretization D_1. We observe that in the low-frequency region $\omega < 30$, where the eigenvalues overlap (see figure 7*a*), the value of ϵ remains above $\epsilon > 10^{-8}$, which indicates that the computed eigenvalues are robust quantities. Note that if μ exactly corresponds to an eigenvalue, we numerically obtain, as expected, tiny values of ϵ, i.e. $\epsilon < 10^{-15}$. We do not see these values in figure 7(*d*) because ϵ has been evaluated only on a relatively coarse mesh in the (ω, σ) plane. None of these points obviously was very close to an eigenvalue. Hence, figure 7(*d*) has to be considered as a 'background' value of ϵ. It corresponds actually to a quality measure of the computed eigenvalues: if the background value of ϵ is very small, say $\epsilon < 10^{-12}$, then the eigenvalues found in this region are not very robust and the whole region may actually be quasi-eigenvalues; if the background ϵ is larger, say $\epsilon > 10^{-8}$, then the eigenvalues are robust and different shifts should recover the same eigenvalue. Coming back to the description of figure 7(*d*), we can see that the background ϵ reaches extremely small values in the region where the high-frequency eigenvalues did not overlap in figure 7(*a*). The solid line indicates for example the isocontour $\epsilon = 10^{-12}$: any value μ below this curve corresponds to an eigenvalue of $\widetilde{\boldsymbol{A}} + \delta\widetilde{\boldsymbol{A}}$ with a tiny matrix perturbation $\||\delta\widetilde{\boldsymbol{A}}|\|_{\boldsymbol{Q}} \leqslant 10^{-12}$. It is conceivable that the shift-invert technique used to extract the eigenvalues introduces such minute perturbations. Hence, the whole area below the solid line has to be considered as quasi-eigenvalues. Figure 7(*e*), which is concerned with the same plot but for discretization D_2 (more extended domain), exhibits a similar behaviour. Yet, it is seen that for frequencies $\omega > 30$, the ϵ values are up to two or three orders of magnitude smaller than those obtained for discretization D_1. Hence, the more extended the domain, the more sensitive the eigenvalues. As a consequence, the isoline $\epsilon = 10^{-12}$ has moved toward smaller damping rates ($-\sigma \approx 11$–12), which is consistent with the location of the non-overlapping eigenvalues in figure 7(*b*). In the case of a shorter domain (figure 7*f*), the ϵ values are much higher and always lay above 10^{-7} for $-\sigma < 18$. This shows that the computed discrete eigenvalues are robust quantities in the case of a shorter domain, in agreement with the overlapping eigenvalues shown in figure 7(*c*). When considering shorter domains, we actually remove a large part of strongly amplified perturbations, which are triggered upstream and which grow exponentially in the downstream direction.

We will now analyse in the case of short domains the effect of the left (z_b) and right (z_f) boundary locations on the eigenvalue spectra. For this, we have compared in figure 8 the spectra related to discretization D_4 with those obtained for discretizations D_5, D_6 and D_7, in which the left and/or right boundaries have slightly been moved upstream or downstream. The figure shows a close-up view, within $30 < \omega < 120$, of the eigenvalues that have been obtained with the shift $s = 60i$. Note that we have checked that all discretizations D_4 to D_7 yield overlapping eigenvalues in this region when different shifts are used (as in figure 7*c*). We can see that each discretization yields a different branch of eigenvalues and that each branch displays different amplification rates, different frequencies and different distances in frequency between two successive eigenvalues. This shows that, despite the fact that the eigenspectra are more robust in the case of shorter domains (the 'background' value of ϵ is at least equal to 10^{-7} in the region of the computed eigenvalues), the eigenspectra
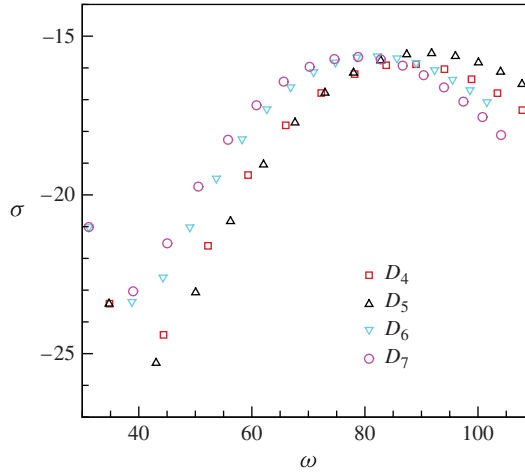
FIGURE 8. (Colour online) Comparison between eigenvalue spectra obtained for discretizations D_4, D_5, D_6 and D_7. Here $Re = 1600$.

remain very sensitive to the locations of the left and right boundaries. It is therefore impossible to define a unique set of eigenvalues and in particular frequencies which are intrinsic to the flow. We believe that it is unlikely that an argument based on a series of eigenvalues obtained for $z_b = 4$ and $z_f = 8$, as promoted by Boyer *et al.* (2013*a*,*b*), may explain the discrete frequency selection mechanism observed in flow induced by radial wall injection.

The analysis of the effect of the discretization order reveals (not shown here) that second-order eigenvalue computations yield a spectrum qualitatively similar to that obtained with a first-order discretization and that the values of ϵ remain quantitatively unchanged, indicating that ϵ is a robust quantity. Considering figure 7(*a,b,d,e*), it seems that $\epsilon = 10^{-12}$ approximately corresponds to the value where non-overlapping eigenvalues are obtained. Note that this threshold value is not universal but dependent on the numerical techniques that were used. Yet, the computed values of ϵ are robust (as shown above), so that the region of quasi-eigenvalues defined by $\epsilon < 10^{-12}$, has not only a numerical but a true physical sense.

Finally, the computed eigenvalues in regions where $\epsilon < 10^{-12}$ were shown (not shown here) to be 'true' eigenvalues, in the sense that time-marching (4.2) with an initial value equal to the real part of an eigenmode yields a solution displaying a time behaviour consistent with the computed eigenvalue μ. Such results are in agreement with those of Chedevergne *et al.* (2012) and Boyer *et al.* (2013*a*).

6. Pseudo-resonance

In this section, after a brief introduction of the singular value decomposition of the resolvent (§ 6.1), we analyse the optimal gains (§ 6.2) and singular modes (§ 6.3) of the flow. In particular, we will try to understand if such quantities may help understand the discrete frequency selection mechanism presented in § 4 for the large-scale forcing. We will conclude this section by an assessment of the influence of the Reynolds number (§ 6.4).

6.1. *Singular values of resolvent*

Considering (4.3), we focus on optimal forcings $\hat{f}$ which maximize the response $\hat{u}$ for a given temporal behaviour μ. More precisely, we look for optimal forcings $\hat{f}$ maximizing the gain:

$$G(\hat{f}) = \frac{\hat{u}^* Q_u \hat{u}}{\hat{f}^* Q_f \hat{f}} = \frac{\hat{f}^* R(\mu)^* Q_u R(\mu) \hat{f}}{\hat{f}^* Q_f \hat{f}}. \tag{6.1}$$

Here, Q_u and Q_f are two hermitian matrices defining the precise ratio to be optimized: Q_f is meant to be positive definite whereas Q_u is positive but may have a non-zero null-space. For example, $\hat{u}^* Q_u \hat{u}$ may stand for the energy in some subdomain Ω_u while $\hat{f}^* Q_f \hat{f}$ could be the energy in the whole computational domain $\Omega_f = \Omega$. More information about the choice of relevant norms can be found in Chernyshenko & Baig (2005) and Blesbois *et al.* (2013).

Following Sipp & Marquet (2012), this optimization problem is solved by considering the following generalized hermitian eigenproblem:

$$R(\mu)^* Q_u R(\mu) \hat{f}_i = \lambda_i^2 Q_f \hat{f}_i, \tag{6.2}$$

where λ_i^2 are the optimal gains (λ_i are also called the singular values) ranked by decreasing value $\lambda_1^2 \geqslant \lambda_2^2 \geqslant \cdots$. Here $\hat{f}_i$ are the optimal forcings (the right singular vectors), which constitute an orthonormal basis $\hat{f}_i^* Q_f \hat{f}_j = \delta_{ij}$ where δ_{ij} stands for the Kronecker symbol. The optimal responses (the left singular vectors) are obtained from

$$\hat{u}_i = \lambda_i^{-1} R(\mu) \hat{f}_i. \tag{6.3}$$

It is easy to verify that $\hat{u}_i$ is another orthonormal set of vectors, $\hat{u}_i^* Q_u \hat{u}_j = \delta_{ij}$. The solution of the eigenproblem (6.2) is carried out with a Lanczos method implemented in the ARPACK library (regular mode), while the matrix inverses involved in the resolvent R (see (6.2) and (6.3)) are performed with the MUMPS package. More details on the numerical implementation are given in Sipp & Marquet (2012).

Now, let us show how this decomposition straightforwardly characterizes the frequency response for any given forcing $\hat{f}$ at frequency ω. For this, we consider the optimal gains λ_i, optimal forcings $\hat{f}_i$ and optimal responses $\hat{u}_i$ obtained for $\mu = i\omega$. The expansion of the forcing $\hat{f}$ onto the set of optimal forcings is given as

$$\hat{f} = \sum_{i=1}^N \alpha_i \hat{f}_i, \tag{6.4}$$

where the complex coefficients α_i are readily obtained as the scalar products of the forcing $\hat{f}$ with the corresponding optimal forcings:

$$\alpha_i = \hat{f}_i^* Q_f \hat{f}. \tag{6.5}$$

The flow response is obtained as an expansion in terms of optimal responses

$$\hat{u} = \sum_{i=1}^N \lambda_i \alpha_i \hat{u}_i. \tag{6.6}$$

This relation is central to the whole approach, since for a given forcing $\hat{f}$, it straightforwardly yields the response of the flow $\hat{u}$.
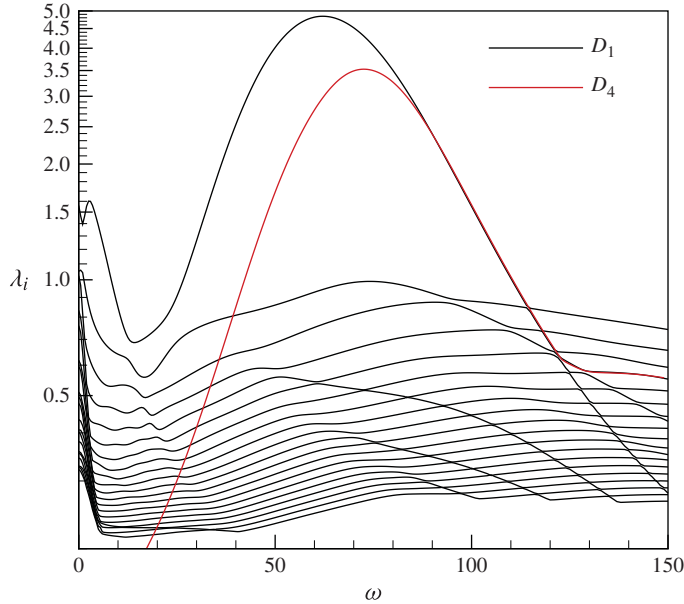
FIGURE 9. The 20 leading singular values λ_i for discretization D_1 (black solid lines) and leading singular value λ_1 for discretization D_4 (red solid line) as a function of frequency ω. $Re = 1600$.

6.2. *Optimal gains*

Figure 9 shows for discretization D_1 (solid black lines) and Reynolds number $Re = 1600$, the 20 largest optimal gains λ_i, solution of (6.2), as a function of frequency ω. We chose for this $\boldsymbol{Q}_f = \boldsymbol{Q}$ and

$$\boldsymbol{u}^* \boldsymbol{Q}_u \boldsymbol{v} = \int_{\Omega} (\bar{u}_r v_r + \bar{u}_z v_z)(z \leqslant 8) r \, \mathrm{d}r \, \mathrm{d}z, \tag{6.7}$$

so that the optimization domain is restricted to $z \leqslant 8$. This has been done to make the results independent of the location of the downstream boundary and of the precise boundary condition that was used. Hence, we look for a forcing that maximizes the energy of the flow response in the domain $z \leqslant 8$. We can see that the first singular value λ_1 is well above the others in the range $30 < \omega < 100$. The leading gain λ_1 features a smooth curve with no distinct peaks. The maximum of this curve is obtained for $\omega \approx 60$–65, indicating that a preferred frequency exists for the extraction of energy within the domain $z \leqslant 8$. This larger gain near $\omega \approx 60$–65 emphasizes a pseudo-resonance mechanism since it cannot be merely explained by the presence of weakly damped eigenvalues in the spectrum of the linearized Navier–Stokes operator (see figure 7a) near these frequencies. We also observe in figure 9 that there are several other branches displaying clear maxima, showing that suboptimal mechanisms to extract energy exist in this flow. Yet, most of the suboptimal branches are rather flat: in the case of backward-facing step flow, such branches were shown to be linked to pure downstream advection of perturbations by the base flow (Dergham, Sipp & Robinet 2013).

In figure 9, we have also represented (in red) the leading singular value for discretization D_4 (for which the computational mesh starts at $z_b = 4$ and ends at $z_f = 8$).
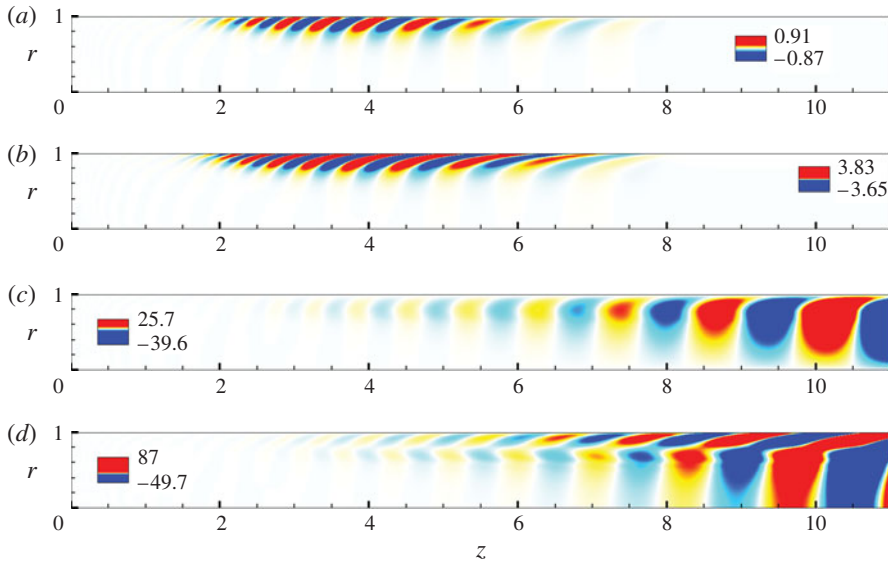
FIGURE 10. Real parts of leading optimal forcing and response at $\omega = 62.5$: (a) $\hat{f}_{1r}$; (b) $\hat{f}_{1z}$; (c) $\lambda_1 \hat{u}_{1r}$; (d) $\lambda_1 \hat{u}_{1z}$. Here $Re = 1600$ and discretization D_1.

We can see that the λ_1 curve is again a smooth curve (as for discretization D_1) despite the fact that the associated eigenspectrum shown in figure 7(c) exhibits clear distinct frequencies: this is due to the fact that the damping rates of the discrete eigenvalues $-\sigma \approx 16$ are higher than the distance between two successive eigenvalues $\Delta\omega = 5$ (for normal matrices, $\lambda_1(\omega)$ is inversely proportional to the distance between $i\omega$ and the closest eigenvalue, see Schmid & Henningson (2001)).

6.3. *Optimal forcings/responses*

The optimal forcing $\hat{f}_1$ and response $\lambda_1 \hat{u}_1$ related to the maximum value of the singular value λ_1 obtained for $\omega = 62.5$ are depicted in figure 10(a–d) by the isocontours of the real part of their radial and axial components. The leading optimal perturbation $\hat{f}_1$ is localized in the region $2 < z < 6$, close to the injecting wall. It is characterized by a series of elongated flow structures that lay against the shear, which are characteristic of the Orr mechanism (Orr 1907). The induced optimal response $\lambda_1 \hat{u}_1$ features vortical structures which get stronger as we move downstream. Upstream near $z \approx 4$, they are located close to the injecting wall, but their size increases as we move downstream and the vortical structures extend up to the channel axis when $z \geqslant 8$. The streamwise wavelength of the structures is seen to increase with z: this stems from the fact that the phase speed of the perturbations (equal to the local axial wavelength times the frequency) reflects the downstream advection velocity of the base flow, which dramatically increases with z due to the radially injected flow.

To further analyse the spatial locations of the leading optimal forcing $\hat{f}_1$ and response $\lambda_1 \hat{u}_1$, we consider the axial energy density function, defined for a given structure $\boldsymbol{a}$ as $\|\boldsymbol{a}\|_{z_0} = \left(\int_{r=0}^{r=1} (\|\boldsymbol{a}(r, z_0)\|^2 r \, dr) \right)^{1/2}$, where at a given point (r, z), $\|\boldsymbol{a}(r, z)\|^2 = a_r^* a_r + a_z^* a_z$. This quantity has been represented for $0 \leqslant \omega \leqslant 115$
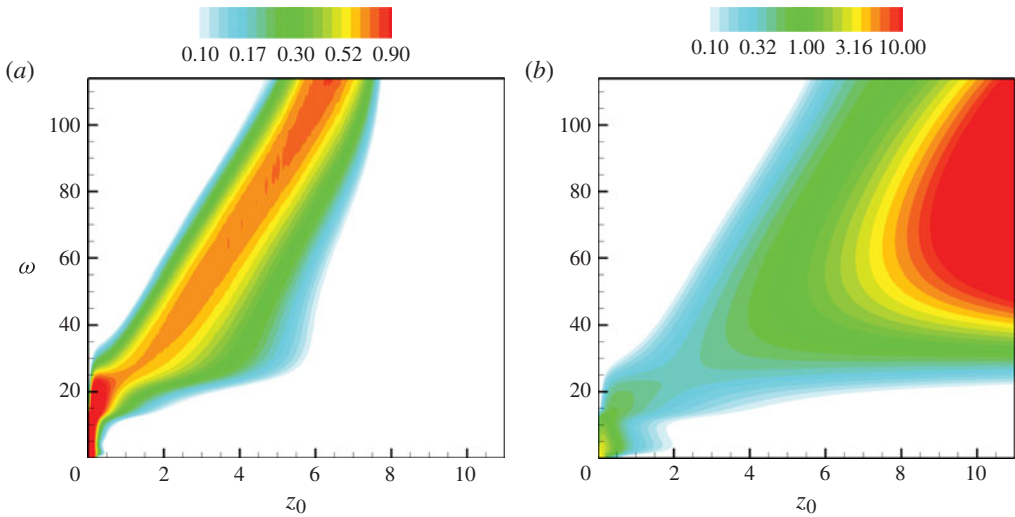
FIGURE 11. Density function for the leading optimal forcing and response: (*a*) $\|\hat{\boldsymbol{f}}_1\|_{z_0}$; (*b*) $\|\lambda_1\hat{\boldsymbol{u}}_1\|_{z_0}$. Here $Re = 1600$ and discretization D_1.

in figure 11, both for the leading optimal forcing (*a*) and response (*b*). We can immediately see that, similarly to the leading optimal gain curve, all curves are smooth as a function of ω with no discrete peaks. We observe that the optimal forcing is always located upstream and the optimal response downstream. This is reminiscent of the strong convective non-normality of the flow, a concept introduced by Marquet *et al.* (2009). Sipp & Marquet (2012) showed in the case of boundary-layer flow subjected to Tollmien–Schlichting instabilities that, for a given frequency ω, the maximum of $\|\hat{\boldsymbol{f}}_1\|_{z_0}$ and $\|\lambda_1\hat{\boldsymbol{u}}_1\|_{z_0}$ as a function of z_0 correspond to the location of branch I and branch II, respectively (in a local spatial stability framework, these correspond to the upstream and downstream points of zero spatial amplification rate). In figure 11(*a,b*), we can see that branch I slightly moves downstream when the frequency increases and that the flow remains convectively unstable whatever the downstream position so that branch II does not exist: for $\omega > 20$, the optimal response is always strongest at the downstream boundary. These results are in agreement with the local stability analyses performed by Griffond *et al.* (2000). Also, Sipp & Marquet (2012) showed that the streamwise density function of $\lambda_1\hat{\boldsymbol{u}}_1$ is related to the results given by an e^N method, which consists of integrating in the streamwise direction the local spatial amplification rate at a given frequency. This link is confirmed here, since figure 11(*b*) is strongly reminiscent of the e^N results shown in Griffond *et al.* (2000).

Let us make a final comment on the λ_1 curve shown with a red solid line in figure 9. We can see that in the case of a computational mesh starting at $z_b = 4$ (discretization D_4), the leading optimal gain coincides with the one obtained with discretization D_1 only for frequencies satisfying $\omega > 80$. As shown in figure 11(*a*), the optimal forcings for $\omega < 80$ are precisely located within the region $z < 4$, a region that has been removed in discretization D_4. Hence, discretization D_4 is accurate only for perturbation frequencies $\omega > 80$, for which the optimal forcings obtained with discretization D_1 are all located within $z > 4$.
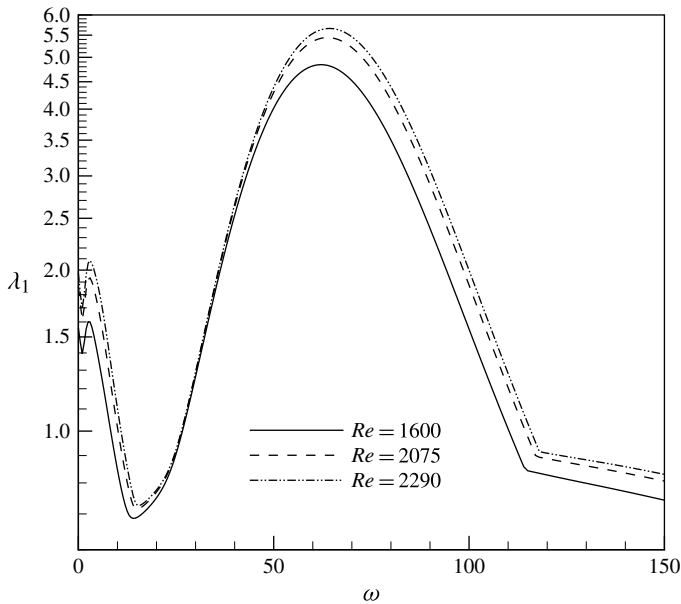
FIGURE 12. First singular value for $Re = 1600, 2075, 2290$. Discretization D_1.

6.4. *Reynolds number influence*

The dependence of the leading optimal gain with respect to the Reynolds numbers Re is studied in figure 12. For each Reynolds number, $Re = \{2075; 2290\}$, we consider the appropriate base flow and solve the eigenvalue problem (6.2) for varying numbers of $\mu = i\omega$. Results show that the optimal gains only slightly increase with the Reynolds number. This is in agreement with the inviscid nature of the instability: using a local stability analysis, Casalis *et al.* (1998) and Griffond *et al.* (2000) have proven that the amplification rates of the instability become nearly independent of the Reynolds number as soon as the Reynolds number reaches a value of 1000. Also, one can note that the frequency displaying strongest optimal gain is slightly shifted to higher values when the Reynolds number is increased.

Comparison of the axial density functions of the optimal forcing and response at $\omega = 62.5$ shows that (figure 13) the optimal forcings are nearly independent of the Reynolds number for $Re \geqslant 1600$, and that the optimal responses become slightly more energetic with increasing Reynolds numbers, in accordance with the fact that the optimal gains slightly increase with the Reynolds number.

7. Discrete frequency selection mechanism with singular vectors

The results presented in the last section have shown that the leading optimal gains, forcings and responses of flow induced by radial wall injection exhibit a smooth behaviour as the frequency is varied. In particular, the leading optimal gain $\lambda_1(\omega)$ does not exhibit any discrete peak, which would have been the case if weakly damped global modes existed in the vicinity of these discrete peaks (which is not the case, see §5). At first glance, such a smooth behaviour of the singular quantities cannot explain the discrete frequency selection mechanism presented in §4 for the large-scale forcing. Further analysis is therefore required.
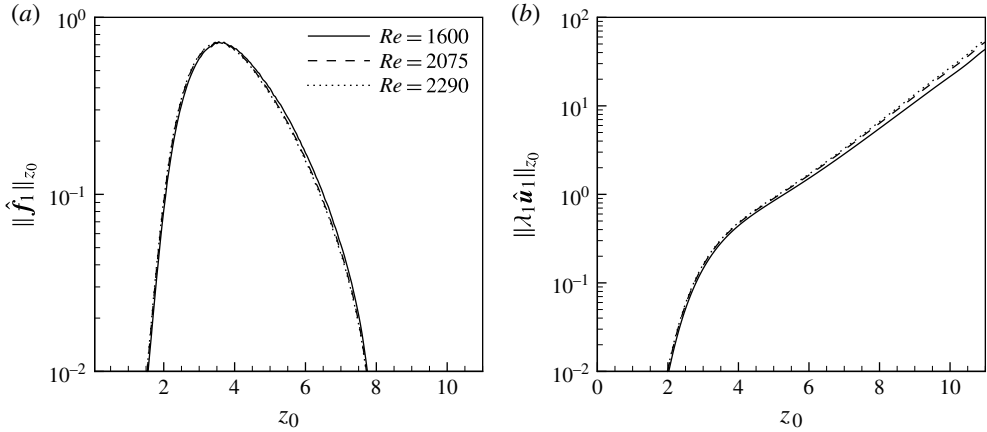
FIGURE 13. Axial energy density function of leading optimal forcing (*a*) and response (*b*) for $\omega = 62.5$ and $Re = 1600, 2075, 2290$. Discretization D_1.

We first recall that the discrete frequency-selection mechanism has been precisely captured by the frequency response computed in (4.3). The information is therefore definitely contained in the matrix–vector product: $\hat{\boldsymbol{u}} = \boldsymbol{R}\hat{\boldsymbol{f}}$, with $\hat{\boldsymbol{f}}$ standing for the fixed large-scale forcing introduced in §4. We also know that the singular value decomposition of $\boldsymbol{R}$, which provides the optimal gains, forcings and responses, yields a very efficient approximation (6.6) of the true frequency response (4.3). It is therefore natural to analyse how many singular values/vectors are needed to reconstruct the true frequency response.

Figure 14(*a,b*) compare the true and approximated frequency responses obtained near the injecting wall ($r_c = 0.9$, $z_c = 8$) (figure 14*a*) and at the centreline of the channel ($r_c = 0$, $z_c = 8$) (figure 14*b*) as a function of frequency. The black, blue and green solid lines respectively refer to approximations (6.6) obtained with $N = 1, 10$ and 20 singular values/modes. We can see that, for both spatial locations, the approximations converge perfectly to the true frequency responses (shown with the red solid line): with $N = 20$ singular values, the approximation in green is nearly identical to the true response. Yet, and most important, it appears that the approximation based on the leading singular value ($N = 1$) is sufficient to capture not only the discrete frequency selection mechanism (all of the frequencies of the peaks are well recovered) but also the overall amplitude of the true frequency response.

Equation (6.6) with $N = 1$ yields the following approximation based on the leading singular value/mode:

$$\hat{\boldsymbol{u}} = \alpha_1 \lambda_1 \hat{\boldsymbol{u}}_1. \qquad (7.1)$$

We recall that all quantities on the right-hand side of this equation depend on the frequency ω and that $\alpha_1 = \hat{\boldsymbol{f}}_1^* \boldsymbol{Q}_f \hat{\boldsymbol{f}}$ corresponds to the projection of the fixed forcing $\hat{\boldsymbol{f}}$ on the leading optimal forcing $\hat{\boldsymbol{f}}_1$. We now focus again on the two spatial locations (r_c, z_c), the first near the injecting wall and the second at the centreline of the channel. Figure 14(*c,d*) respectively depict for these two points a breakdown of $|\hat{\boldsymbol{u}}(r_c, z_c)|$ (which is shown with black solid lines in figure 14*a,b*) into the three coefficients $|\alpha_1|$ (red solid lines in figure 14*c,d*), λ_1 (black dotted lines) and $|\hat{\boldsymbol{u}}_1(r_c, z_c)|$ (black solid lines) as a function of frequency. As already mentioned above, the frequency
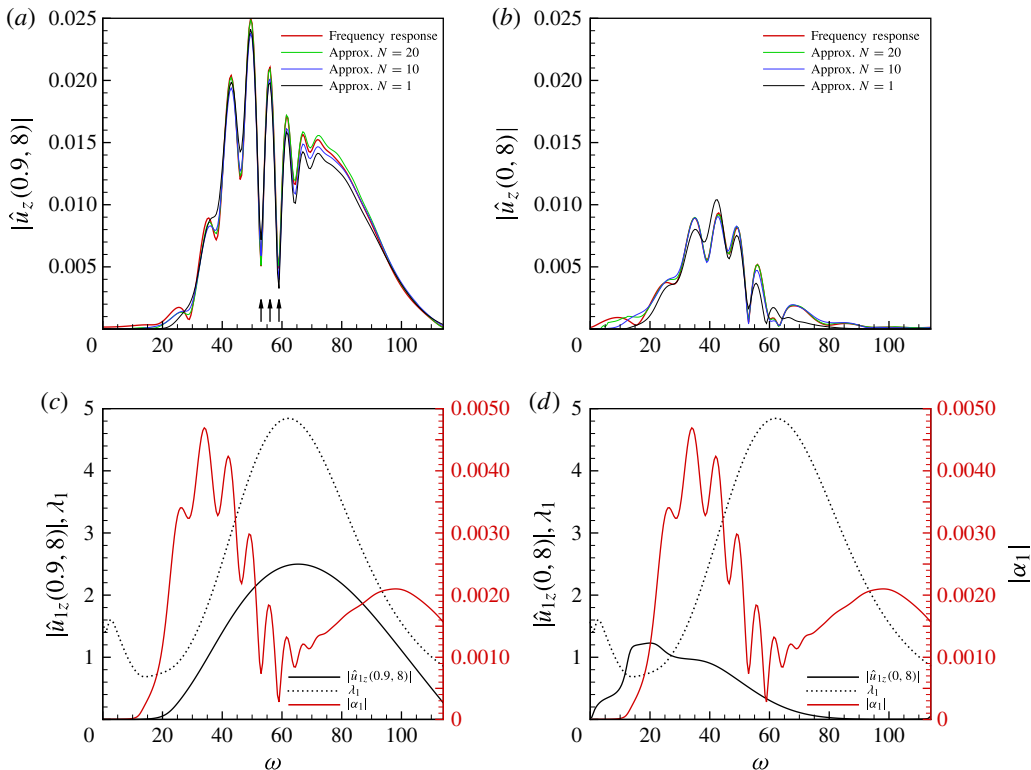
FIGURE 14. (*a,b*) Comparison of true frequency response based on (4.3) with approximations based on $N = 1$, $N = 10$ and $N = 20$ singular modes (see (6.3)). Axial velocity component at (*a*) ($r = 0.9$, $z = 8$) and (*b*) ($r = 0$, $z = 8$). (*c,d*) Analysis of leading order response $\hat{\boldsymbol{u}} = \alpha_1 \lambda_1 \hat{\boldsymbol{u}}_1$ at (*c*) ($r = 0.9$, $z = 8$) and (*d*) ($r = 0$, $z = 8$). Here $Re = 1600$ and discretization D_1.

dependence of $|\hat{\boldsymbol{u}}_1(r_c, z_c)|$ and λ_1 yield smooth curves. One may therefore note that the discrete frequency selection mechanism is due to the $|\alpha_1|$ curve, which exhibits strong oscillations near a series of regularly spaced frequencies. Note that when focusing on just a few spatial points, it may be useful to consider optimization domains restricted only to the vicinity of these points: such an idea was introduced by Chernyshenko & Baig (2005) and may help improve the convergence properties of the series (6.6).

Approximation (7.1) shows that the frequency spectrum $|\hat{\boldsymbol{u}}(\omega)|$ at a given point (r_c, z_c) may be quite complex since it is proportional to three quantities all dependent on the frequency: the optimal gain function $\lambda_1(\omega)$, which does neither depend on the forcing nor on (r_c, z_c), the projection coefficient $|\alpha_1(\omega)|$, which depends on the forcing but not on (r_c, z_c), and $|\hat{\boldsymbol{u}}_1(r_c, z_c, \omega)|$, which depends on (r_c, z_c) and not on the forcing. Hence, for a given forcing, the frequency spectrum at all points in the flow reflects the shape of $\lambda_1(\omega)$ and $|\alpha_1(\omega)|$, but a strong modulation from point to point may be observed due to different shapes of $|\hat{\boldsymbol{u}}_1(\omega)|$. For example, comparing the frequency spectra near the injecting wall and at the centreline of the channel, we observe in figure 14(*a,b*) that the peaks are located at the same frequencies ($\alpha_1(\omega)$), but that the dominant frequencies are within $40 < \omega < 90$ near the injecting wall and within $20 < \omega < 60$ at the centreline of the channel, a difference due to $|\hat{\boldsymbol{u}}_1(\omega)|$.
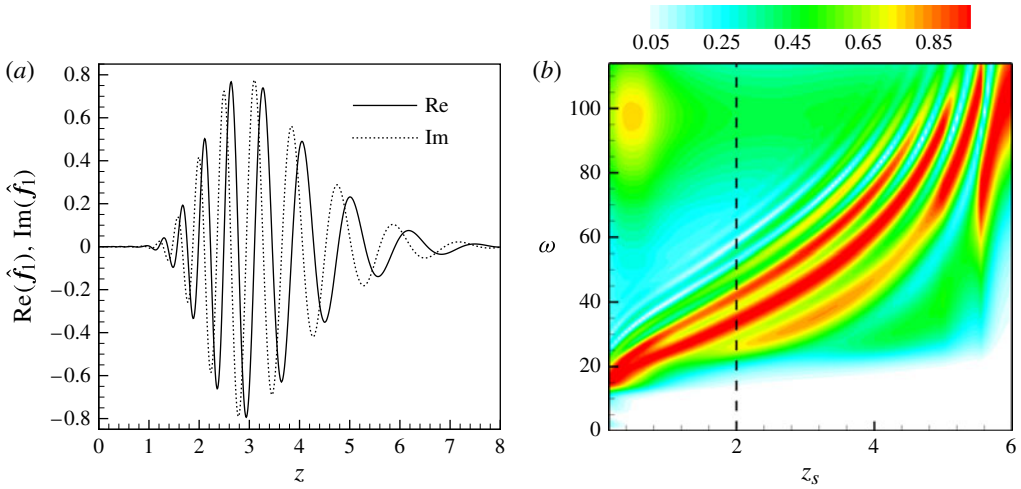
FIGURE 15. (a) Streamwise evolution of the real and imaginary parts of the radial component of the leading optimal forcing at $\omega = 53$ for $r = 0.9$. (b) Isovalues of $|\alpha_1|/(\max_\omega |\alpha_1|)$. The forcing region is located within $(0.90 \leqslant r \leqslant 0.95, z_s \leqslant z \leqslant 6)$. The vertical dashed line refers to the large-scale forcing for which $z_s = 2$. Here $Re = 1600$ and discretization D_1.

In order to better understand the origin of the discrete peaks shown in the $|\alpha_1(\omega)|$ curve of figure 14(c,d), let us introduce a simple one-dimensional model that helps to explain these observations. To start, we note that the leading optimal forcing displays streamwise oscillations, that have been represented in figure 15(a) by the real and imaginary parts of the radial component of the optimal forcing $\hat{f}_{1r}$ at $r_c = 0.9$ for $\omega = 53$. In addition, if larger frequencies are considered, then smaller wavelengths are observed in the optimal forcing. We now consider the following simplified one-dimensional model with the leading optimal forcing $\hat{f}_1 = \sin(kz) + \mathrm{i}\cos(kz)$, which is representative of the above-described optimal forcing, with the real and imaginary parts $1/4$ spatial period out of phase but with a constant amplitude. We then consider a rectangular one-dimensional forcing equal to $\hat{f} = 1$ within $z_s \leqslant z \leqslant z_e$ and zero outside. It is straightforward to show that in this one-dimensional case,

$$|\alpha_1(k)| = (z_e - z_s) \left| \mathrm{sinc} \left[\frac{k(z_e - z_s)}{2} \right] \right| \tag{7.2}$$

where sinc is the cardinal sine function. The $|\alpha_1(k)|$ curve therefore exhibits intense oscillating sidelobes that are characteristic of the sinc function. This behaviour is linked to the Fourier transform of a rectangular pulse, which is equal to the sinc function: similar observations are made in the signal processing field where the windowing of a periodic signal by a square window creates strong oscillations. Finally, oscillations in the $|\alpha_1(k)|$ curve yield similar oscillations in the $|\alpha_1(\omega)|$ curve since the wavenumber k of the leading optimal forcing increases with the frequency ω. Hence, strong peaks of the projection coefficient $|\alpha_1(\omega)|$ are expected for some regularly spaced frequencies ω. Note that the picture in figure 14 is slightly more complex, since the oscillations do not reach the zero value: this is due to the

strong amplitude variations displayed by $\hat{f}_1$ (see figure 15a), that have not been taken into account by the simplified model.

In §4, we showed that the narrow and large-scale forcings did not exhibit the same qualitative behaviour, the frequency response of the narrow forcing being smooth with no frequency selection. We have analysed the results of the narrow forcing in a similar way. We have observed (not shown here) that the projection coefficient $|\alpha_1|$ is a smooth curve as a function of the frequency ω. This may again be understood in light of the simplified model for which the projection coefficient is given in (7.2). Considering the range of frequencies within $20 < \omega < 80$ (which correspond to the amplified frequencies), the streamwise wavenumber k of the optimal forcing varies within $k_{20} < k < k_{80}$. The constants k_{20} and k_{80} designate the streamwise wavenumbers of the optimal forcings at frequencies $\omega = 20$ and $\omega = 80$. The phase ϕ within the sinc function then varies within $(z_e - z_s)k_{20}/2 < \phi < (z_e - z_s)k_{80}/2$. For the narrow forcing, $z_e - z_s$ is 13 times smaller than in the case of the large-scale forcing. Therefore, the variations of the phase ϕ become too small (within the range of amplified frequencies) to induce oscillations in the projection coefficient $|\alpha_1(\omega)|$.

We will now verify that the frequency-selection mechanism described just above is at play for a wide variety of forcings. As a first step toward exploring a broader set of forcings, we have computed the frequency dependence of the projection coefficient $|\alpha_1(\omega)|$ for forcings beginning at z_s and ending at $z_e = 6$, with $0 < z_s < 6$ ($\hat{f}_r = 1$ and $\hat{f}_z = 0$ within $(0.90 \leqslant r \leqslant 0.95, z_s \leqslant z \leqslant 6)$). In figure 15($b$), we have represented isovalues of $|\alpha_1|$ within the (z_s, ω) plane. Note that the coefficient $|\alpha_1|$ has been normalized for each forcing z_s by its maximum value over all frequencies, $\max_\omega |\alpha_1(\omega)|$, so that the coefficient has a maximum value equal to 1 in each vertical slice. We can see a great variety of behaviours with respect to the starting position z_s of the forcing structures. It is seen that peaks in the frequency spectrum cover the entire frequency range $20 < \omega < 120$. Such a graph needs to be interpreted in connection with location of branch I: the general trend seen in figure 15(b) follows closely those shown in figure 11(a). This stems from the fact that the starting z_s position of the forcing needs to be located near branch I to obtain quick variations of the projection coefficient $|\alpha_1|$ as a function of frequency.

Such results underline the major role played by the spatial structure of the forcing in the existence and location of discrete peaks in the frequency spectrum of flow induced by radial injection. Within the various forcing structures that have been explored here, it seems that discrete peaks in the frequency spectrum may be encountered quite often. Note, however, that the discrete peaks do not exist in the case of a smoother (in z) forcing. It is the rectangular shape of the forcing that is at the very origin of the spiky spectrum. Hence, for a noise amplifier flow to exhibit discrete peaks in the frequency response, the shape of the forcing structure is as important as its location and extension.

8. Comparison with experimental study

We will now investigate how the present results compare with the experimental investigations led by Cerqueira *et al.* (2009) on the VALDO set-up, that has been devised to investigate the pressure oscillations induced by aeroacoustic phenomena inside solid propellant rocket motors. With an ambient air apparatus, the radius of the channel of 30 mm and injection velocities of $V_{inj} = 0.83$ and 1.10 m s^{-1} correspond to $Re = 1660$ and $Re = 2200$, respectively. The laminar–turbulent transition occurs around $z \approx 10$. Similar results were obtained in other cold-gas apparatus experiments
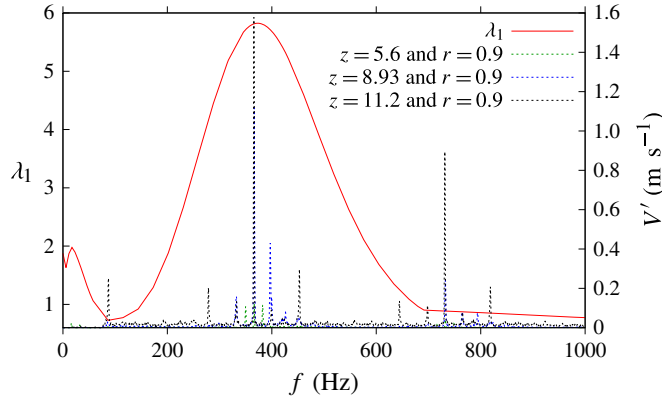
FIGURE 16. Comparison between the leading optimal gain (obtained for $Re = 2075$) and the experimental spectrum for $Re = 2200$. Discretization D_1 for stability computation. Experimental results reproduced from Cerqueira *et al.* (2009).

(see Varapaev & Yagodkin 1969; Dunlap *et al.* 1990). It was checked that the mean flows in the experiment by Cerqueira *et al.* (2009) favourably compare with the Taylor–Culick analytical solution for $Re \geqslant 1660$ and $5.6 \leqslant z \leqslant 12.67$.

In the experiment, the forcing structures $\hat{\boldsymbol{f}}$ are of course unknown and a precise comparison of experimental results with approximation (7.1) is not possible. Here, we just compare the frequency dependence of λ_1 (obtained at $Re = 2075$) with a spectrum of fluctuating velocity component obtained at three distinct streamwise locations, $(r_c = 0.9, z_c = 5.6)$, $(r_c = 0.9, z_c = 8.93)$ and $(r_c = 0.9, z_c = 11.2)$, for $Re = 2200$ (as shown in §6.4, this slight mismatch in Reynolds number is not an issue since singular quantities only weakly depend on the Reynolds number for $Re \geqslant 1600$). Results displayed in figure 16 show that experimental velocity fluctuation frequencies arise in the vicinity of the maximum of $\lambda_1(\omega)$. Obviously the discrete peaks cannot be recovered here since they are due to the projection coefficient $|\alpha_1|$ and not to the optimal gain λ_1, which only determines the overall shape of the spectrum. The second series of peaks observed at higher frequencies are harmonics of the first series of peaks: they are probably associated with nonlinear effects that cannot be captured by the present linear approach.

Figure 17 displays a comparison between radial profiles of root-mean-square (RMS) velocity fluctuations obtained in the experiment (for $Re = 1660$) and of the leading optimal response $|\hat{\boldsymbol{u}}_1|$ obtained at $\omega = 62.5$ (for $Re = 1600$). The overall amplitude of the response has been fixed at $z = 7.93$ to match the experimental results. The radial profile at $z = 9.57$ has been deduced from the structure of the optimal response. Although some discrepancies are observed, velocity fluctuation distributions from the global linear stability analysis are found to be in fairly good agreement with the experimental data. This statement is true both for the radial distribution at a given station and for the streamwise amplification.

The present results indicate that we face a true receptivity problem, in which the central component is the external forcing. This external forcing may actually stem from various physical origins in the experiment: quality of the air, geometrical defects, details about how the radial flow is injected in the chamber, nonlinear interactions with acoustics, etc. Note, however, that the flow being laminar in the experiment up to $z \approx 10$, forcings stemming from turbulent motions $\boldsymbol{f}' \approx -\boldsymbol{u}' \cdot \nabla \boldsymbol{u}'$ (such as those considered in turbulent shear flows by McKeon & Sharma (2010)) should not be
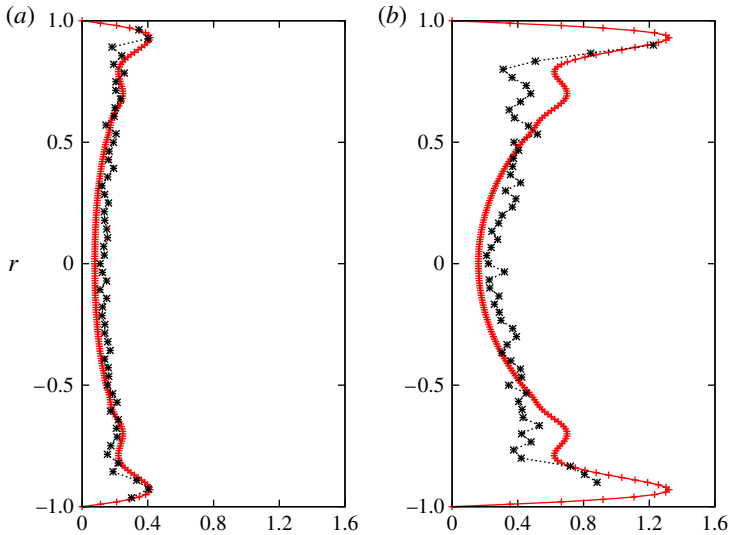
FIGURE 17. Comparison of radial profiles of optimal response $|\hat{\boldsymbol{u}}_1|$ obtained at $\omega = 63.25$ (for $Re = 1600$) with RMS of velocity fluctuations (obtained for $Re = 1660$). Two sections are investigated: (*a*) $z = 7.93$, where the overall amplitude of the response has been chosen to match the experimental profile; and (*b*) $z = 9.57$, where the profile of the response has been deduced from the structure of the leading optimal response. Discretization D_1 for stability computation. Experimental results reproduced from Cerqueira *et al.* (2009).

considered in the present experiment. In the next section, we will briefly discuss how a large-scale external forcing of rectangular shape (that has been recognized to be a key feature to obtain spiky spectra) could in principle be obtained in an experiment.

9. Discussion on the relevancy of large-scale forcing in the experiment

We consider in this section the interaction of an acoustic wave with an elongated wall defect of rectangular shape. We will start with the case of a two-dimensional boundary layer, before discussing again the case of flow induced by radial wall injection.

The forthcoming development is a generalization of Crouch (1992). We consider a steady laminar two-dimensional boundary-layer flow and an acoustic wave of small amplitude $\epsilon \ll 1$ and frequency ω_f interacting with a defect at the wall. Here, the defect will have an elongated rectangular shape, of small and constant height $\delta \ll 1$. The flowfield $\boldsymbol{q} = (u_x, u_y, p)^{\mathrm{T}}$ is given by

$$\boldsymbol{q}(x, y, t) = \underbrace{\boldsymbol{q}_0(x, y)}_{\text{base-flow}} + \underbrace{\delta \boldsymbol{q}_\delta(x, y)}_{\text{defect}} + \underbrace{\left[\epsilon e^{i\omega_f t} \boldsymbol{q}_\epsilon(x, y) + \text{c.c.}\right]}_{\text{acoustic wave}} + \underbrace{\left[\delta \epsilon e^{i\omega_f t} \boldsymbol{q}_{\delta\epsilon}(x, y) + \text{c.c.}\right]}_{\text{interaction}} + \cdots .$$

(9.1)

The defect-induced base-flow modification $\boldsymbol{q}_\delta(x, y)$ is equal at the wall to $-\nabla \boldsymbol{q}_0 \cdot \boldsymbol{n}$ at the defect's location and zero on the rest of the wall ($\boldsymbol{n}$ is the unit vector in the y direction). Here $\boldsymbol{q}_\delta(x, y)$ therefore approximately exhibits a rectangular shape close to the wall. In the free stream, the acoustic wave $e^{i\omega_f t} \boldsymbol{q}_\epsilon(x, y)$ converges toward the plane wave solution ($u_{\epsilon, x} = 1, u_{\epsilon, y} = 0$), while close to the wall viscous effects generate a Stokes layer. The nonlinear interaction between the defect and the acoustic wave

is obtained at order $\delta\epsilon$, with the computation of $\boldsymbol{q}_{\delta\epsilon}(x, y)$. This component, which oscillates at the frequency ω_f, is determined by two forcings: first, at the wall $\boldsymbol{q}_{\delta\epsilon}$ must be equal to $-\nabla\boldsymbol{q}_\epsilon \cdot \boldsymbol{n}$ at the defect's location and zero on the rest of the wall (modification of the acoustic wave due to the defect); second, it is forced in the field by the nonlinear interaction between the defect-induced base-flow modification $\boldsymbol{q}_\delta$ and the acoustic wave $\boldsymbol{q}_\epsilon$. Due to the rectangular shape of the defect, these two forcings also exhibit a nearly rectangular shape. The equation governing $\mathrm{e}^{\mathrm{i}\omega_f t}\boldsymbol{q}_{\delta\epsilon}$ may actually correspond to the forced linearized Navier–Stokes equation considered in (2.4): the two above-mentioned forcing terms may stand for $\boldsymbol{f}'$ so that $\boldsymbol{f}'$ could exhibit a shape close to the large-scale forcing considered in the present paper if acoustic waves interacting with wall defects were considered. The response $\boldsymbol{q}_{\delta\epsilon}(x, y)$ is strongest (and so is the receptivity of the flow) when the forcing frequency ω_f of the acoustic wave is closest to the peak of the optimal gain curve $\lambda_1(\omega)$. If the wall defect is elongated and displays a rectangular shape, the equivalent forcing that accounts for the wall defect will look very much like the large-scale forcing of this article. We therefore expect a spiky spectrum in the case of an acoustic wave interacting with an elongated wall defect within a boundary layer.

We think that an analogous mechanism may exist in the case of flow induced by radial wall injection. The acoustic wave is now replaced by a longitudinal acoustic mode in a pipe (a closed-form solution that accounts for the interaction with the Taylor–Culick flow and the lateral walls can be found in Majdalani & Van Moorhem (1998)). If again an elongated defect of rectangular shape is considered, the problem should be equivalent, as in the boundary-layer case, to a large-scale forcing of rectangular shape. Hence, an elongated wall defect of rectangular shape could generate a spiky spectrum. Note, however, that the present proposal did not convince one of the referees of this paper, who found it unphysical in the context of solid propellant rocket motors.

10. Conclusion

We have shown in the present article that for certain external forcing structures flow induced by radial wall injection may display discrete peaks in the frequency spectrum. This has been established both by performing a forced linearized DNS simulation and by computing the frequency response of the flow. We have then tried to explain these observations with global stability analyses. We have first shown that the eigenvalues of the Jacobian, which are located in the frequency range of interest, are ill-behaved and extremely sensitive to numerical discretization details if the computational domain is large. On the other hand, as suggested by Boyer *et al.* (2013*a*,*b*), these eigenvalues are more robust in the case of shorter domains. Yet, they still exhibit a strong sensitivity to the location of the left and right boundaries, which makes it impossible to identify a unique set of discrete frequencies in the Jacobian matrix that is intrinsic to the flow. These conclusions have been supported by an analysis of the ϵ-pseudo-spectrum. We have shown in particular that the 'background' value of ϵ is a quality measure of the computed eigenvalues: if ϵ is below 10^{-8} in some region, then the computed eigenvalues in this region are not anymore robust. We believe that eigenvalues are not the good quantities to focus on to study the dynamics of flow induced by radial wall injection. We rather think that in globally stable cases, especially when the convective non-normality is extremely strong, as is the case here, it is a better idea to consider the singular values and vectors of the resolvent matrix. These are robust quantities which are far less sensitive to discretization

details. Moreover, this decomposition yields a simple approximation of the resolvent operator, and therefore of the frequency response of the flow, which is based on the leading optimal gain, forcing and response. We have shown by analysing this approximation in the case of the large-scale forcing that it is the projection coefficient of the forcing onto the leading optimal forcing that is responsible for the discrete peaks in the frequency response. This result is rather surprising since globally stable flows are related to amplifier flows, which are usually characterized by smooth broadband frequency spectra (in the case of broadband excitations). Flow induced by radial wall injection is an example of amplifier flow, which may display frequency spectra with discrete peaks, despite the fact that the forcing is white. What is even more striking is that this phenomenon is not linked to weakly damped eigenmodes (the leading optimal gain curve is smooth and presents a single peak) but to the projection coefficient of the external forcing onto the leading optimal forcing. Hence, the structure of the external forcing is a key quantity in such a dynamics showing that the frequency selection mechanism is not intrinsic but dependent and determined by the noise environment. In this respect, flow induced by radial wall injection is a true noise amplifier.

We make the following conclusions with respect to the sensitivity issue. We have shown that the eigenvalue spectrum is extremely sensitive and should not be considered in systems which display strong convective instabilities, as is the case here. Yet, this does not mean that time marching the Navier–Stokes equations will result in a sensitive solution. Only the eigenvalues are sensitive but the time evolution of the solution, the singular vectors or the optimal initial perturbations remain robust quantities. Note however that the singular values depend on the choice of the optimization domain. Our conclusion is that the optimization domain (and, therefore, the computational domain in a DNS simulation) should start at the head end if the low frequencies of the instability need to be accounted for. For the location of the right boundary of the optimization domain, the choice is guided by the region where linear growth is expected: for example, in the VALDO experiment, transition occurs around $z \approx 10$. Hence, it seems natural to choose 8 or 9 as the right boundary of the optimization domain to study the linear amplification mechanisms in this set-up.

Results and techniques were presented here in the context of flow induced by radial wall injection. In particular, we have shown how spiky spectra may be obtained in the case of large-scale coherent forcings of rectangular shape. We have also provided a physical scenario explaining how such forcings may be generated from the interaction of a longitudinal acoustic mode and an elongated defect at the wall. More work is actually required to confirm the relevancy of this proposal in the case of flow in solid propellant rocket motors. In particular, a precise characterization of the noise environment is needed to make progress. Finally, it is important to stress that the present study is relevant for all amplifier flows and that discrete peaks in frequency spectra may be observed in such flows due to the shape, extension and location of the external forcings. The present study also yields some clues for the analysis of flows displaying strongly sensitive unstable global modes, as presented in the introduction. It is suggested here to compute the 'background' value of ϵ in the region around the unstable global modes. If this background ϵ is very small, then minute perturbations of the Jacobian operator (changes in boundary conditions, meshing, order of spatial discretization, location of boundaries) can strongly affect the computed eigenvalues. It is important to realize that this is not only a numerical but a true physical issue: flows displaying non-robust unstable eigenvalues should in principle exhibit some dynamical features that are very sensitive, for example to the chosen experimental apparatus, to the noise environment, etc.

REFERENCES

AKERVIK, E., EHRENSTEIN, U., GALLAIRE, F. & HENNINGSON, D. S. 2008 Global two-dimensional stability measures of the flat plate boundary-layer flow. *Eur. J. Mech. (B/Fluids)* **27** (5), 501–513.

ALIZARD, F. & ROBINET, J.-C. 2007 Spatially convective global modes in a boundary layer. *Phys. Fluids* **19** (11), 114105.

AMESTOY, P. R., DUFF, I. S., KOSTER, J. & L'EXCELLENT, J.-Y. 2001 A fully asynchronous multifrontal solver using distributed dynamic scheduling. *SIAM J. Matrix Anal. Applic.* **23** (1), 15–41.

BARBAGALLO, A., SIPP, D. & SCHMID, P. J. 2009 Closed-loop control of an open cavity flow using reduced-order models. *J. Fluid Mech.* **641**, 1–50.

BARBAGALLO, A., SIPP, D. & SCHMID, P. J. 2011 Input–output measures for model reduction and closed-loop control: application to global modes. *J. Fluid Mech.* **685**, 23–53.

BLACKBURN, H. M., BARKLEY, D. & SHERWIN, S. J. 2008 Convective instability and transient growth in flow over a backward-facing step. *J. Fluid Mech.* **603**, 271–304.

BLESBOIS, O., CHERNYSHENKO, S. I., TOUBER, E. & LESCHZINER, M. A. 2013 Pattern prediction by linear analysis of turbulent flow with drag reduction by wall oscillation. *J. Fluid Mech.* **724**, 607–641.

BOYER, G., CASALIS, G. & ESTIVALÈZES, J. L. 2013a Stability analysis and numerical simulation of simplified solid rocket motors. *Phys. Fluids* **25**, 084109.

BOYER, G., CASALIS, G. & ESTIVALÈZES, J. L. 2013b Stability and sensitivity analysis in a simplified solid rocket motor flow. *J. Fluid Mech.* **722**, 618–644.

CANTWELL, C. D., BARKLEY, D. & BLACKBURN, H. M. 2010 Transient growth analysis of flow through a sudden expansion in a circular pipe. *Phys. Fluids* **22**, 034101.

CASALIS, G., AVALON, G. & PINEAU, J. P. 1998 Spatial instability of planar channel flow with fluid injection through porous walls. *Phys. Fluids* **10**, 2558–2568.

CERQUEIRA, S., AVALON, G. & FEYEL, F. 2009 An experimental investigation of fluid–structure interaction inside solid propellant rocket motors. *AIAA Paper* 2009-5427, Proceedings of the AIAA/ASME/SAE/ASEE, 45th Joint Propulsion Conference and Exhibit, Denver, Colorado.

CHEDEVERGNE, F. 2007 Instabilités intrinsèques des moteurs à propergol solide. PhD thesis, Ecole Nationale Supérieure de l'Aéronautique et de l'Espace (ENSAE), Toulouse, France.

CHEDEVERGNE, F., CASALIS, G. & FÉRAILLE, T. 2006 Biglobal linear stability analysis of the flow induced by wall injection. *Phys. Fluids* **18**, 014103.

CHEDEVERGNE, F., CASALIS, G. & MAJDALANI, J. 2012 Direct numerical simulation and biglobal stability investigations of the gaseous motion in solid rocket motors. *J. Fluid Mech.* **706**, 190–218.

CHERNYSHENKO, S. I. & BAIG, M. F. 2005 The mechanism of streak formation in near-wall turbulence. *J. Fluid Mech.* **544**, 99–131.

CROUCH, J. D. 1992 Localized receptivity of boundary layers. *Phys. Fluids* A **4** (7), 1408–1414.

CULICK, F. E. C. 1966 Rotational axisymmetric mean flow and damping of acoustic waves in a solid propellant rocket. *AIAA J.* **4** (8), 1462–1464.

CULICK, F. E. C. 2006 Unsteady motions in combustion chambers for propulsion systems. *NATO Science and Technology Organization – RTO AGARDograph* RTO-AG-AVT-039 AC/323(AVT-039)TP/103.

DAVIS, T. A. & DUFF, I. S. 1997 An unsymmetric-pattern multifrontal method for sparse LU factorization. *SIAM J. Matrix Anal. Applics.* **18** (1), 140–158.

DERGHAM, G., SIPP, D. & ROBINET, J.-C. 2013 Stochastic dynamics and model reduction of amplifier flows: the backward facing step flow. *J. Fluid Mech.* **719**, 406–430.

DUNLAP, R., BLACKNER, A. M., WAUGH, R. C., BROWN, R. S. & WILLOUGHBY, P. G. 1990 Internal flow field studies in a simulated cylindrical port rocket chamber. *J. Propul. Power* **6** (6), 690–704.

EHRENSTEIN, U. & GALLAIRE, F. 2005 On two-dimensional temporal modes in spatially evolving open flows: the flat-plate boundary layer. *J. Fluid Mech.* **536**, 209–218.

GARNAUD, X., LESSHAFFT, L., SCHMID, P. J. & HUERRE, P. 2013a Modal and transient dynamics of jet flows. *Phys. Fluids* **25** (4), 044103.

GARNAUD, X., LESSHAFFT, L., SCHMID, P. J. & HUERRE, P. 2013b The preferred mode of incompressible jets: linear frequency response analysis. *J. Fluid Mech.* **716**, 189–202.

GRIFFOND, J., CASALIS, G. & PINEAU, J. P. 2000 Spatial instability of flow in a semiinfinite cylinder with fluid injection through its porous walls. *Eur. J. Mech. (B/Fluids)* **19**, 69–87.

ILAK, M., SCHLATTER, P., BAGHERI, S. & HENNINGSON, D. S. 2012 Bifurcation and stability analysis of a jet in cross-flow: onset of global instability at a low velocity ratio. *J. Fluid Mech.* **696**, 94–121.

MAJDALANI, J. & VAN MOORHEM, W. 1998 Improved time-dependent flowfield solution for solid rocket motors. *AIAA J.* **36** (2), 241–248.

MARQUET, O., LOMBARDI, M., CHOMAZ, J.-M., SIPP, D. & JACQUIN, L. 2009 Direct and adjoint global modes of a recirculation bubble: lift-up and convective non-normalities. *J. Fluid Mech.* **622**, 1–21.

MARQUET, O., SIPP, D., CHOMAZ, J.-M. & JACQUIN, L. 2008 Amplifier and resonator dynamics of a low-Reynolds-number recirculation bubble in a global framework. *J. Fluid Mech.* **605**, 429–443.

MATSUMOTO, J. & KAWAHARA, M. 2000 Stable shape identification for fluid–structure interaction problem using mini element. *Trans. ASME J. Appl. Mech.* **3**, 263–274.

MCKEON, B. J. & SHARMA, A. S. 2010 A critical-layer framework for turbulent pipe flow. *J. Fluid Mech.* **658**, 336–382.

MOARREF, R. & JOVANOVIĆ, M. R. 2012 Model-based design of transverse wall oscillations for turbulent drag reduction. *J. Fluid Mech.* **707**, 205–240.

MONOKROUSOS, A., AKERVIK, E., BRANDT, L. & HENNINGSON, D. S. 2010 Global three-dimensional optimal disturbances in the blasius boundary-layer flow using time-steppers. *J. Fluid Mech.* **650**, 181–214.

ORR, W. M. F. 1907 Stability or instability of the steady motions of a perfect liquid. *Proc. R. Irish Acad.* **27**, 9–69.

SANMIGUEL-ROJAS, E., DEL PINO, C. & GUTIERREZ-MONTES, C. 2010 Global mode analysis of a pipe flow through a 1:2 axisymmetric sudden expansion. *Phys. Fluids* **22** (7), 071702.

SCHMID, P. J. & HENNINGSON, D. S. 2001 *Stability and Transition in Shear Flows*. Springer.

SHARMA, A. S. & MCKEON, B. J. 2013 On coherent structure in wall turbulence. *J. Fluid Mech.* **728**, 196–238.

SIPP, D. & MARQUET, O. 2012 Characterization of noise amplifiers with global singular modes: the case of the leading-edge flat-plate boundary layer. *Theor. Comput. Fluid Dyn.* **27**, 617–635.

SIPP, D., MARQUET, O., MELIGA, O. & BARBAGALLO, A. 2010 Dynamics and control of global instabilities in open flows: a linearized approach. *Appl. Mech. Rev.* **63**, 030801.

TAYLOR, G. I. 1956 Fluid flow in regions bounded by porous surfaces. *Proc. R. Soc. Lond.* **234**, 456–475.

TREFETHEN, L. N. & EMBREE, M. 2005 *Spectra and Pseudospectra: The Behavior of Non-normal Matrices and Operators*. Princeton University Press.

TREFETHEN, L. N., TREFETHEN, A. E., REDDY, S. C. & DRISCOLL, T. A. 1993 Hydrodynamic stability without eigenvalues. *Science* **261** (5121), 578–584.

VARAPAEV, V. N. & YAGODKIN, V. I. 1969 Flow stability in a channel with porous walls. *Izv. Akad. Nauk SSSR Mekh. Zhidk. Gaza* **4** (5), 91–95.

VUILLOT, F. 1995 Vortex shedding phenomena in solid rocket motors. *J. Propul. Power* **11**, 626–639.